

Modeling the Gas Flow in the Bar of NGC 1365

R. Zánmar Sánchez

J. A. Sellwood

*Department of Physics and Astronomy, Rutgers University,
136 Frelinghuysen Road, Piscataway, NJ 08854*

zanmar,sellwood@physics.rutgers.edu

B. J. Weiner

*Steward Observatory, Department of Astronomy, University of Arizona,
933 N. Cherry Ave., Tucson, AZ 85721*

bjw@as.arizona.edu

and

T. B. Williams

*Department of Physics and Astronomy, Rutgers University,
136 Frelinghuysen Road, Piscataway, NJ 08854*

williams@physics.rutgers.edu

ABSTRACT

We present new observations of the strongly-barred galaxy NGC 1365, including new photometric images and Fabry-Perot spectroscopy, as well as a detailed re-analysis of the neutral hydrogen observations from the VLA archive. We find the galaxy to be at once remarkably bi-symmetric in its I-band light distribution and strongly asymmetric in the distribution of dust and in the kinematics of the gas in the bar region. The velocity field mapped in the H α line reveals bright HII regions with velocities that differ by 60 to 80 km s⁻¹ from that of the surrounding gas, which may be due to remnants of infalling material. We have attempted hydrodynamic simulations of the bar flow to estimate the separate disk and halo masses, using two different dark matter halo models and covering a wide range

of mass-to-light ratios (Υ) and bar pattern speeds (Ω_p). None of our models provides a compelling fit to the data, but they seem most nearly consistent with a fast bar, corotation at $\sim 1.2r_B$, and $\Upsilon_I \simeq 2.0 \pm 1.0$, implying a massive, but not fully maximal, disk. The fitted dark halos are unusually concentrated, a requirement driven by the declining outer rotation curve.

Subject headings: galaxies: individual (NGC 1365) — galaxies: spiral — galaxies: photometry — dark matter — ISM: kinematics and dynamics

1. Introduction

The centrifugal balance of the circular flow pattern in a near-axisymmetric spiral galaxy yields a direct estimate of the central gravitational attraction as a function of radius. However, the division of the mass giving rise to that central attraction into separate dark and luminous parts continues to prove challenging. The radial variation of the circular speed simply does not contain enough information to allow a unique decomposition between the baryonic mass, which has an uncertain mass-to-light ratio, Υ , and the dark halo, whose density profile is generally described by some adopted parametric function (van Albada *et al.* 1985; Lake & Feinswog 1989; Barnes, Sellwood & Kosowsky 2004).

Predictions for Υ from stellar population synthesis models that match broad-band colors (e.g. Bell *et al.* 2003) are useful, but not precise. Despite intense effort, they are still sufficiently uncertain to be consistent with both maximum and half-maximum disk, which is the range of disagreement (e.g. Sackett 1997; Bottema 1997; Sellwood 1999). McGaugh (2005) argues that the values can be refined by minimizing the scatter in the Tully-Fisher and/or mass discrepancy-acceleration relation.

A number of dynamical methods have been employed to break the disk-halo degeneracy. Casertano (1983), Bosma (1998), and others have suggested that the slight decrease in orbital speed near the edge of the optical disk of a bright galaxy – the “truncation signature” – could be used as an indicator of disk Υ , but in practice it does not provide a tight constraint. Athanassoula, Bosma & Papaioannou (1987) and Fuchs (2003) attempt to constrain the disk mass using spiral structure theory. Bottema (1997) and Verheijen *et al.* (2004) measure the vertical velocity dispersion of disk stars in a near face-on galaxy, which they assume has the same mean thickness of similar galaxies seen edge-on (Kregel, van der Kruit & de Grijs 2002), to constrain the disk mass. A similar approach is reported by Ciardullo *et al.* (2004) using velocity measurements of individual planetary nebulae.

One of the most powerful, although laborious, methods for barred galaxies was pi-

oneered by Weiner, Sellwood & Williams (2001), who made use of the additional information in the driven non-circular motions caused by the bar. By modeling the observed non-axisymmetric flow pattern of the gas in a 2-D velocity map, they were able to determine the mass-to-light ratio of the visible disk material. They found that the luminous disk and bar contributed almost all the central attraction in NGC 4123 inside ~ 10 kpc, requiring the dark halo to have a very low central density. Weiner (2004) reports a similar result for a second case, NGC 3095. The method has also been applied by Pérez *et al.* (2004) for several barred galaxies and by Kranz *et al.* (2003) who modeled motions caused by spiral arms. Bissantz, Englmaier & Gerhard (2003) present a similar study for the Milky Way. Earlier studies (*e.g.* Duval & Athanassoula 1983) did not attempt to separate the disk from the dark matter halo (see Sellwood & Wilkinson 1993, for a review). Here, we apply the (Weiner *et al.* 2001) method to the more luminous barred galaxy NGC 1365 in the Fornax cluster.

As one of the most apparently regular, nearby barred spiral galaxies in the Southern sky, NGC 1365 was selected by the Stockholm group for an in-depth study (see *e.g.* Lindblad 1999). Hydrodynamic models of the bar flow pattern were already presented by (Lindblad, Lindblad & Athanassoula 1996), based mainly on the velocities of emission-line measurements from many separate long-slit observations. Jörsäter & van Moorsel (1995, hereafter JvM95) present a kinematic study using the 21 cm line, which suggests that the galaxy is somewhat asymmetric in the outer parts, where the shape of the rotation curve is hard to determine. Sandqvist *et al.* (1995) find substantial amounts of molecular gas, but only within 2 kpc of the nucleus, which is resolved in interferometric observations (Sakamoto *et al.* 2007) into a molecular ring in the center plus a number of CO hot spots. Galliano *et al.* (2005) have found previously unknown MIR sources in the inner $10''$ around the AGN. They are able to correlate some of these MIR sources with radio sources, which they interpret in terms of embedded star clusters because of the lack of strong optical counterparts. Jungwiert, Combes & Axon (1997) present H-band photometry of the bright inner disk, finding an elongated component in the central region suggesting that the NGC 1365 is a double-barred galaxy, although they note that the light in this component is not as smooth as in their other nuclear bar cases. Laine *et al.* (2002) also classify it as a double barred galaxy. However, Emsellem *et al.* (2001) and Erwin (2004) argue against a nuclear bar, citing an HST NICMOS image which resolves the feature into a nuclear spiral. Emsellem *et al.* (2001) also present stellar kinematics from slit spectra using the ^{12}CO bandhead. They propose a model for the inner 2.5 kpc of NGC 1365 consisting of a decoupled nuclear disk surrounded by spiral arms within the inner Lindblad resonance (ILR) of the primary bar. Beck *et al.* (2005) observed NGC 1365 in radio continuum at $9''$ - $25''$ resolution and find radio ridges roughly overlapping with the dust lanes in the bar region. They propose that magnetic

forces can control the flow of gas at kiloparsec scales.

Here we present new photometric images, a full 2-D velocity map of the $H\alpha$ emission, and a reanalysis of the neutral hydrogen data from JvM95. We also compare many hydrodynamic models to these new data in an effort to determine the separate disk and dark halo masses in this galaxy.

2. Observations

The Weiner *et al.* (2001) method requires both broad band photometry, to estimate the distribution of visible matter, and a high spatial resolution velocity map to determine the projected non-axisymmetric flow pattern in the barred region. While not absolutely essential, knowledge of the rotation curve at larger radii is helpful to estimate the total central attraction. Velocity maps using the 21cm line of neutral hydrogen have lower spatial resolution but extend to larger radii, and are therefore an ideal complement to the optical data.

Here we adopt the distance to NGC 1365 of 18.6 Mpc, as deduced from Cepheid variables by Madore *et al.* (1999). At this distance, $1''$ corresponds to 90.2 pc.

2.1. Surface Photometry

Observations of NGC 1365 were made on the night of 1999 Jan 24 with the Swope 1 m telescope at Las Campanas Observatory. The LCO Tek#5 2048×2048 pixel CCD was used with a pixel scale of $0.''70$ and a field of view of $24'$. We obtained 3×10 minute offset exposures in each of the V & I filters. The seeing was approximately $1.''6$. We reduced the images with IRAF¹ with the standard procedure: subtraction of overscan, bias, and flat-fielding with twilight flats. The LCO CCD detector exhibits fringing and illumination gradients in the I filter. These were removed by constructing a supersky image by combining all the available I-band images taken throughout the night and subtracted from NGC 1365 I-band image. Photometric standard stars from Landolt (1992) were observed at several times during the night and used to derive extinction coefficients.

The resulting calibrated I-band image is presented in the upper panel of Figure 1. We

¹IRAF is distributed by NOAO, which is operated by AURA, Inc., under a cooperative agreement with the National Science Foundation.

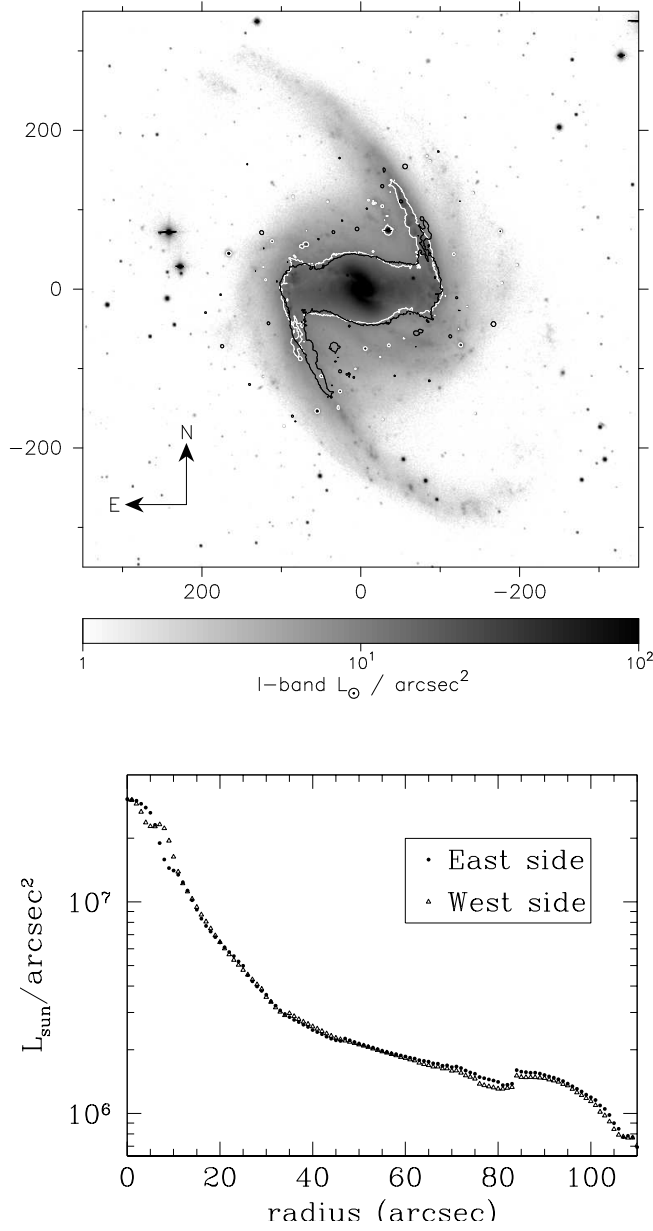


Fig. 1.— *Upper:* A 700'' square region with the I-Band image of NGC 1365 showing intensity on a log scale. The intensity range does not represent the full range and has been chosen to reveal the spiral and bar structures most clearly (*i.e.* the center of the galaxy has a luminosity of $\sim 3 \times 10^7 L_{\odot} / \text{arcsec}^2$). A white contour with intensity $1.2 \times 10^6 L_{\odot} / \text{arcsec}^2$ has been plotted to outline the bar. The black contour is the same as the white but rotated by 180° ; the similarity of the two contours shows the remarkable 2-fold symmetry of the bar. Subsequent figures show this isophote for reference drawn from a 2-fold rotationally averaged image. *Lower:* Surface brightness profiles for the east and west sides of the bar estimated independently. The length of the semimajor axis of the bar is 100''.

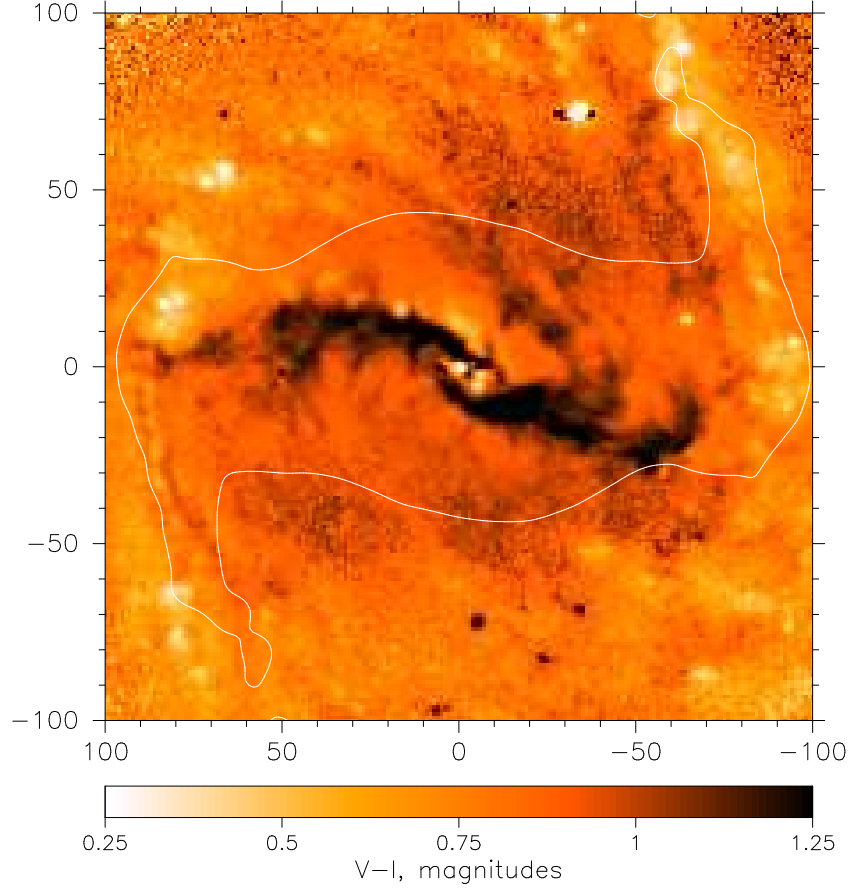


Fig. 2.— A V-I color map of the central $200''$ square region of NGC 1365. Dust lanes are clearly visible on the leading sides of the bar. The isophote from Fig. 1 is included for reference. Note the absence of symmetry in the dust lanes; that on the west side lies farther from the bar major-axis.

have drawn a single isophotal contour and redrawn the same contour rotated through 180° in order to show the symmetry of the bar light distribution. This particular isophote shows the approximate size of the bar, as determined below. We see that the east side of the bar is marginally fatter, at this isophote level, than is the west, but the shape of the bar is remarkably symmetric. In subsequent figures we draw, as a reference, a slightly smoothed version of this isophote from the 2-fold rotationally averaged I-band light distribution.

The lower panel in Figure 1 presents independent estimates of the surface brightness profile for the left and right side of the bar, constructed as follows. We ran the IRAF-ellipse tool on a version of the I-band image smoothed to $3''$, to find a set of isophotal ellipses with position angle and ellipticity as free parameters, but with a fixed center. We then used the same generated ellipses on the original I-band image to find the mean intensity for the east and west sides independently. This analysis reveals that the light distribution is

indeed highly symmetric. The apparent discontinuity in the light profiles at $r \sim 85''$ is due to variations in the fitted ellipticity caused by a number of bright HII regions near the end of bar.

The strong dust lanes in the bar, and other places, are easily visible in the V-I color map of NGC 1365 (Figure 2). As usual, the dust lanes are on the leading side of the bar (which rotates clockwise if the spiral arms are assumed to trail). Despite the evident 2-fold symmetry of the bar, the dust lanes are clearly not symmetric; the strongest dust features on the west side lie farther towards the leading edge of the bar than those on the east. This asymmetric extinction could be the cause of the mild asymmetry in the bar light (Fig. 1) noted above.

Since the NE side of the galaxy is approaching while the SW receding, trailing spiral arms imply that the NW of the galaxy is tipped towards us. Assuming the redder regions in the color map indicate diffuse dust, there appears to be more extinction on the near (NW) side than on the far (SE) side, which is consistent with expectations for a moderately inclined disk (*e.g.* Binney & Merrifield 1998, §4.4.1). Holwerda *et al.* (2005) present a detailed study of dust extinction in part of NGC 1365.

We deproject the galaxy to obtain a face-on surface brightness profile, adopting the projection geometry indicated by the kinematic maps presented in §4: position angle (hereafter PA) = 220° and inclination $i = 41^\circ$. We estimate $R_{23.5} = 348'' \simeq 31.4$ kpc in the I-band, which is comparable to B magnitude $R_{25} = 337''$ de Vaucouleurs *et al.* (1991), and an exponential scale length for the disk of $r_d \simeq 6.5$ kpc. We estimate the total magnitude within $R_{23.5}$ to be 8.2 in I and 9.4 in V, without any extinction corrections. For our modeling of the potential from the I band, we apply an internal extinction correction $A_{\text{int}} = -1.0 \log(b/a)$ from Giovanelli *et al.* (1994) and a galactic extinction from Schlegel, Finkbiner & Davis (1998) for a total correction of -0.16 at I.

We estimated the size of the bar by fitting ellipses to the deprojected I-band image at a number of isophote levels. Ideally, one hopes for an abrupt change in the ellipticity and PA of the radial profiles at the transition between the bar and the disk. The spiral arms, however, force the PA to vary continuously and broaden the ellipticity peak somewhat (Wozniak *et al.* 1995). We estimate the deprojected bar semi-major axis to be $114'' \lesssim r_B \lesssim 127''$, where the lower limit is the radius of maximum ellipticity, 0.63, and the upper limit is radius at which the PA begins to change sharply. This range is in agreement with the value of $r_B = 120'' \pm 10''$ estimated by Lindblad, Lindblad & Athanassoula (1996) using Fourier moment decomposition, and hereafter we adopt their value $r_B = 120'' = 10.8$ kpc as the bar semi-major axis. While physically large, $r_B \simeq 1.66r_d$, which is typical (Erwin 2005).

In this work, we use our I-band image as a measure of the light from the old disk stars. Although far less problematic than in the V-band, some residual dust obscuration slightly attenuates the I-band light. As the opacity of dust is still lower in infrared light, it might be argued that a better estimate of the underlying stellar light distribution could be obtained from J, H, or K-band images. However, the NIR bands are not a panacea as the light in these bands is more seriously affected by AGB stars and hot dust in HII regions, as may be seen by the lumpiness of the 2MASS (Strutskie *et al.* 1997) K-band image. In addition, no available NIR detector is large enough to cover this galaxy well out to the sky without mosaicking, and no existing near infrared image is deep enough (*e.g.* 2MASS) to yield the accurate measure of the outer disk surface brightness profile we require. Furthermore, de Jong (1996) shows that the dependence of the I-band surface brightness on age and star formation history is only slightly stronger than for the K-band. We therefore adopt our I-band image as the best available estimator of the underlying disk light down to very low surface brightness levels.

2.2. Fabry-Perot Imaging Spectroscopy

NGC 1365 was observed in the $H\alpha$ line on the nights of 1993 November 3-4 with the CTIO 1.5m telescope using the Rutgers Imaging Fabry-Perot interferometer.² A Tektronix 1024×1024 CCD detector was used with $0.''98$ pixels. The field of view of the etalon was 7.8 in diameter. Hourly calibrations were taken in order to correct for temporal drifting of the wavelength zero point and optical axis center.

The first night of the observations was photometric but the second night was plagued with intermittent cloud, and three exposures had to be discarded. The remaining NGC 1365 observations consist of 16 separate 10-minute exposures spanning 17.4 \AA in steps of $\sim 1.2 \text{ \AA}$ (54 km s^{-1}) and covering a range of velocities from 1010 to 2031 km/s. The reduction methods are similar to those described elsewhere (Palunas & Williams 2000; Weiner *et al.* 2001). The images were reduced with IRAF: overscan subtraction, bias, and flat fielding. After the removal of cosmic rays, the images were spatially registered and sky subtracted to build the data cube. The typical seeing as measured from foreground stars was around $2.4''$. Sky transparency variations occurred throughout the observation and are a major source of uncertainties in line profiles (Williams *et al.* 1984). We measure the flux of brightest, isolated foreground star in the field of view and scale the frames to a common transparency. Corrections never exceed 3%.

Four frames of our cube seem to be mildly contaminated by sky lines $\lambda = 6604.13$

²CTIO is operated by AURA under contract to the NSF.

and $\lambda = 6596.64 \text{ \AA}$ produced by air OH rotation-vibration transitions (Osterbrock & Martel 1992). A model of the sky ring can be easily constructed because the spectral width of sky lines is very narrow and we should recover only the unresolved instrumental Voigt profile. Nevertheless, the peak intensity of the sky ring is hard to determine because of the confusion with the light of the embedded galaxy. We tried a range of peak intensity values and convinced ourselves that it is no more than 4-5 counts above the background level. Subtraction of these sky rings eliminated spurious fits in the faint outskirts of the galaxy and had no noticeable effect on the velocity fits within the galaxy.

The Fabry-Perot has a spectral resolution of 2.5 \AA at $\text{H}\alpha$ or $\text{FWHM} \simeq 150 \text{ km s}^{-1}$. The spectral profile was approximated with a Voigt function with Gaussian $\sigma_G = 21.6 \text{ km s}^{-1}$ and Lorentzian $\sigma_L = 61.4 \text{ km s}^{-1}$. In order to improve the S/N of our line profiles, we combined data from adjacent pixels using a varying Gaussian kernel of up to 5×5 pixels for which the FWHM is adapted depending on the strength of the line. We use only the central pixel when the line is very strong, but bin pixels 3×3 ($\text{FWHM}=1.6''$) for lines of intermediate strength, and use a 5×5 box ($\text{FWHM}=3.3''$) for very weak emission.

Fabry-Perot images are not strictly monochromatic because of the angular dispersion of the instrument. For every pixel, the wavelength is calculated from a quadratic variation with the radial distance from the optical axis determined from calibration lamp exposures. With the fluxes and wavelengths for every pixel, a Voigt function of five parameters can be fitted with least-squares techniques. After some experimentation, we decided to fix the Lorentzian width to the instrumental value and fitted the four remaining parameters: center wavelength (velocity), Gaussian line width, peak intensity of the emission and the continuum level. Figure 3 shows a selection of resultant emission line profiles: (a) and (b) are of very bright HII regions in the spiral arms, (c) and (d) are of bright HII regions in the eastern and western side of the bar respectively, while (e) and (f) are of diffuse emission from the east side of the bar.

Fits to every pixel yield maps of velocity, line strength, line width, continuum level and the estimated uncertainty in each quantity. Figure 5 presents the velocity map; regions where the velocity uncertainty exceeds 20 km s^{-1} are left blank. We illustrate the velocities using 10 colors only so that the interface between two colors marks an isovelocity contour. The dotted outline is the reference isophote of the bar while the two straight solid lines in the outer regions lie along the estimated (see §4) minor axis of the galaxy and help to identify kinks in the velocity field inside the bar.

Figure 4 presents a comparison between our Fabry-Perot velocity measurements and the long slit measurements using $\text{H}\alpha$ and $\text{H}\gamma$ from Lindblad *et al.* (1996), taken from their Fig 2.e. Their slit was centered on bright HII region L33 and runs along the South-North

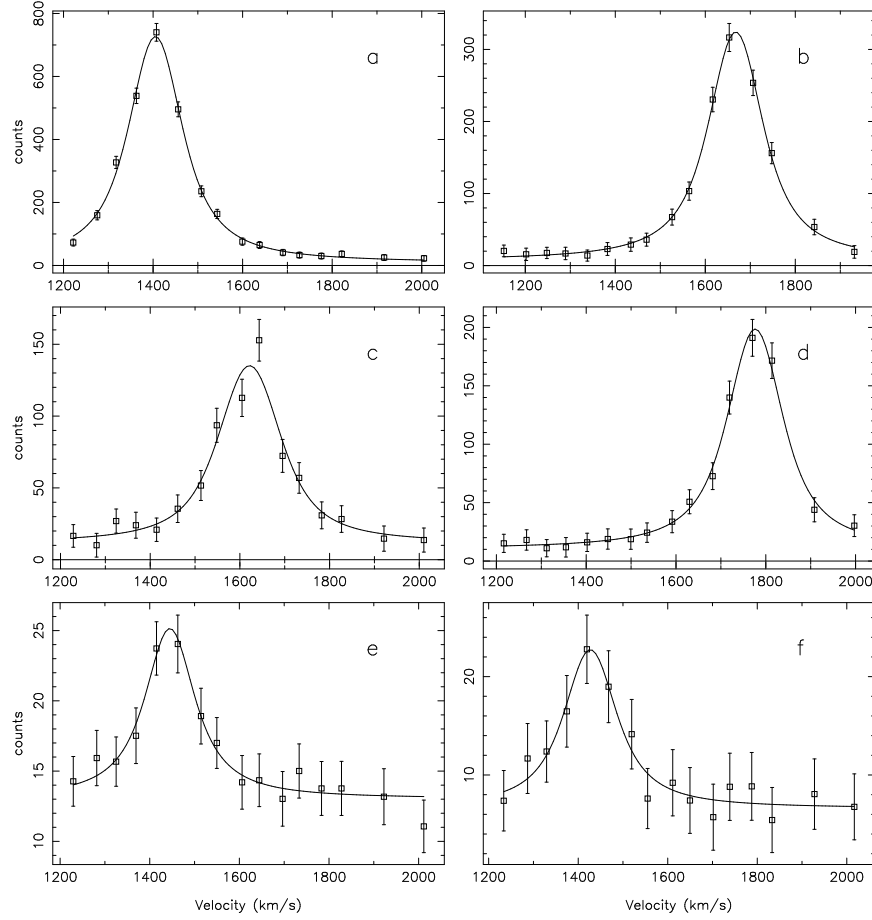


Fig. 3.— Example line profiles. *a.)* and *b.)* Bright HII region on spiral arm. *c.)* and *d.)* Bright HII regions from east and west side of the bar respectively; *c.)* is from the region labeled R2 in Fig. 5. *e.)* and *f.)* Diffuse emission from east side of the bar.

direction with the zero point of the velocity set to 1630 km/s. We also find very good agreement (within $1 - \sigma$) between our measured velocities for other bright HII regions L2, L3, L4, L29, L32, as labeled by Alloin *et al.* (1981), and HII region containing supernova 1983V. Our estimates for the nucleus and L1 differ from theirs by ~ 40 km/s, which is not surprising since NGC 1365 is a Seyfert galaxy and several authors (Phillips *et al.* 1983; Edmunds *et al.* 1988; Lindblad *et al.* 1996) have detected splitting of the high excitation line [OIII]. Double-valued velocities are thought to arise from a disk component and a bipolar hollow conical outflow, as first proposed by Phillips *et al.* (1983).

The velocity map reveals steep gradients in the bar region, especially on the leading edges, where the dust lanes are also found, as has been reported previously (Jörsäter *et al.* 1984; Lindblad *et al.* 1996; Teuben *et al.* 1986, and references therein). These steep gradients are strongly asymmetric as is clear in our velocity map. The velocity jumps on the west side

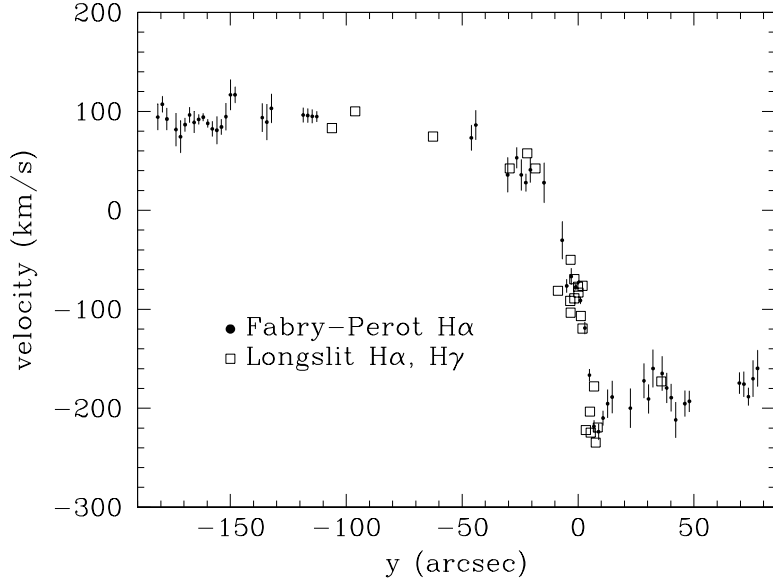


Fig. 4.— Comparison between line-of-sight velocities from Fabry-Perot data (filled points) and the long slit measurements (open symbols) from Lindblad *et al.* (1996). Data from their Fig. 2e are based on the $H\alpha$ and $H\gamma$ lines from a slit positioned in the N-S direction and centered on the bright HII region L33.

of the bar extend farther to the leading side of the bar, consistent with the asymmetric arrangement of the dust lanes. The asymmetry can also be seen in Fig. 4 of Lindblad *et al.* (1996), although based on a rather sparse spatial coverage (interpolated map from 35 slits).

The line profile (Fig. 3c) of the bright HII region on the east side of the bar labeled R2 in Fig. 5 (offset from the nucleus $x = \Delta\alpha \cos\delta = 54.60''$, $y = \Delta\delta = 13.88''$), is not well fitted by a single broadened velocity, but seems to be more complex. Furthermore, the mean fitted velocity at this location differs substantially from that of the faint emission in the surrounding pixels (see inset of Fig. 5). Other bright HII regions on the east side of the bar (*e.g.* R1 at $x = 45.90''$, $y = 20.64''$ and R3 at $x = 55.33''$, $y = -0.84''$) show similar anomalies.

In order to quantify the velocity difference between these three bright regions and that of the surrounding diffuse gas, we fit a bi-linear velocity gradient to the diffuse emission over a small square patch (20×20 pixels) surrounding each bright region. The interpolated velocity at the center of the HII regions differs by between 60 & 80 km/s from the measured value. These complicated profiles may result from disturbance by infalling gas, as discussed in §3.

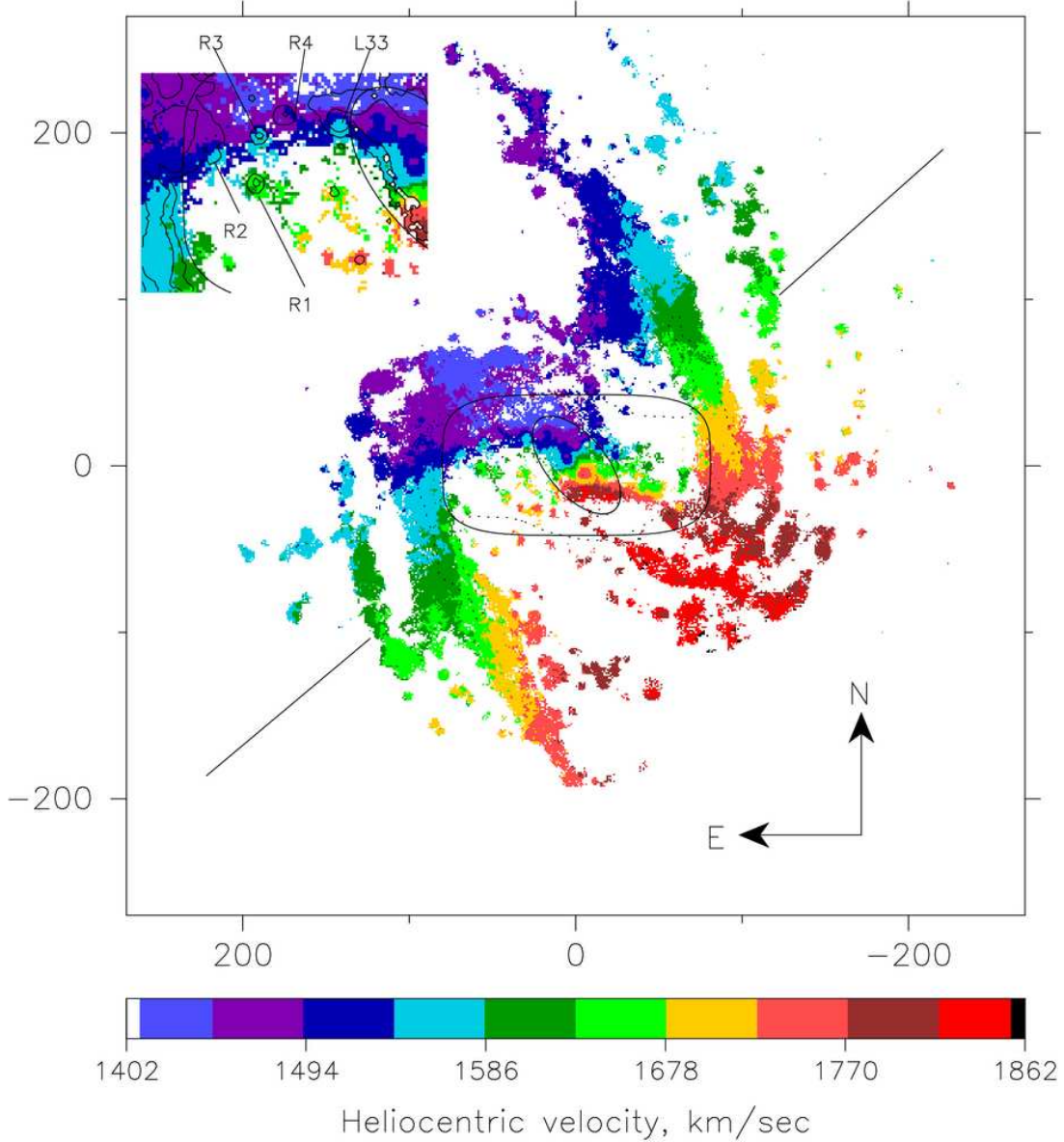


Fig. 5.— The velocity map of NGC 1365 from Fabry-Perot observations of the $H\alpha$ emission line. The color map has been binned in 10 colors to outline velocity contours. The dotted line shows the contour from Fig. 1. The closed solid curves are described in §6.1. The upper-left inset shows an enlargement of the east side of the bar with contours of intensity to show the positions of several labeled bright HII regions.

2.3. HI radio observations

NGC 1365 was observed at the VLA in the HI 21 cm line in 1986 (see JvM95) for 48 hours in three different configurations: BnA, CnB and DnC. The observations were collected on 11 different days; further details of the observations are given in JvM95. Motivated by

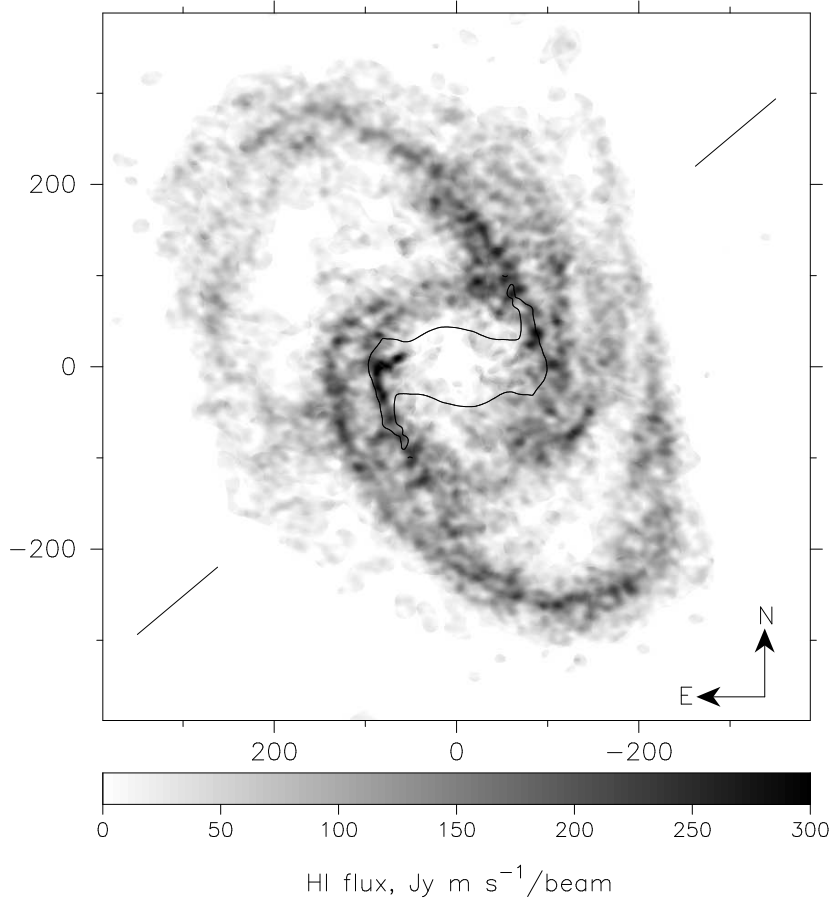


Fig. 6.— The distribution of neutral hydrogen, from the velocity-integrated 21-cm surface brightness. The beam size is $10.3'' \times 9.7''$

improvements in numerical routines in AIPS and by the puzzling declining rotation curve reported by these authors, RZS spent a summer at NRAO³ re-analyzing these observations of NGC 1365 under the supervision of Gustaaf van Moorsel.

Data from the different days were reduced independently and then combined in the UV plane using standard AIPS calibration procedures (DBCON, UVLIN). The resulting combined beamsize was $10.3'' \times 9.7''$. Only 31 channels with a corresponding velocity resolution of 20.84 km s^{-1} were used.

An image cube was created with the task IMAGR using robust weighting (see Briggs 1995). Natural and uniform weighting are controlled in AIPS by the robustness parameter

³The NRAO is operated by Associated Universities, Inc., under a cooperative agreement with National Science Foundation.

and we explored the range from -4 (uniform weighting) to 4 (natural weighting) by measuring the RMS of an empty box in the resulting map and by checking the dirty beam size. A robustness of zero gave the best compromise between noise and beam size. The resulting RMS value was 2.7×10^{-4} Jy/Beam and we cleaned our maps to a depth of $1\text{-}\sigma$. Images of HI intensity, velocity field, and velocity dispersion were obtained with XMOM in AIPS after blanking unnecessary channels with the task BLANK.

The velocity-integrated HI distribution is presented in Fig. 6. The eastern spiral arm has a clear double ridge in HI where it joins to the bar, while the inner arm fades farther out. The western arm is also double, possibly even triple, but in this case the innermost arm is that most easily traced to the outer disk. As shown in Fig. 7 of JvM95, the HI distribution extends only slightly farther out than the light; there is very little neutral gas beyond a deprojected radius of $400''$, while we already reported above that $R_{23.5} = 348''$ in the I-band. Furthermore, the outer distribution is asymmetric, with a single spiral arm extending to the NW.

The velocity field mapped in the 21cm line, presented in Fig. 7, is nowhere characterized by a simple planar, near-circular flow pattern. The strong bar and spiral arms produce non-axisymmetric distortions to the flow pattern that are revealed by kinks in the isovelocity contours. Also a mild warp is suggested by the bending of the isovelocity contours towards the north in the north-east side and towards the south in the south-west side of the galaxy. All of these factors conspire to make the rotation curve of NGC 1365 very difficult to determine. JvM95 concluded that the outer disk was strongly warped, leading them to report a steeply declining rotation curve.

3. Asymmetries

While asymmetries of all kinds are evident at larger radii, the inner parts of NGC 1365 are at once remarkably symmetric in the I-band light (Fig. 1), and strikingly asymmetric in the position of the dust lane and gas kinematics. The $H\alpha$ velocities in the bar region also reveal a number of patches of emission with strongly anomalous velocities when compared with the mean flow. These facts point to some kind of on-going disturbance to the gas flow in the inner galaxy that has little effect on the light.

The galaxy is a member of the Fornax cluster; its projected position is near the cluster center, while its systemic velocity differs from the cluster mean by about 200 km/s (Madore *et al.* 1999). Thus the outer parts of NGC 1365 could be affected by the tidal field of the cluster and/or ram-pressure of the intra-cluster gas. However, tidal forces are unlikely

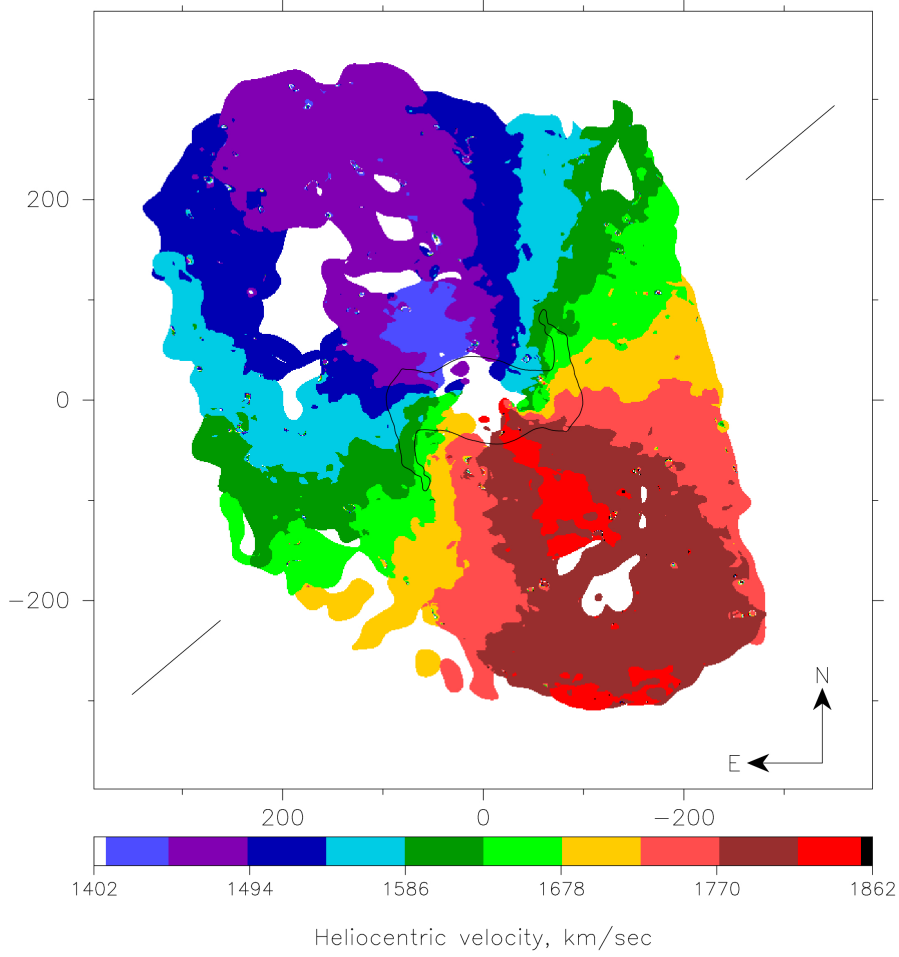


Fig. 7.— The velocity map of NGC 1365 from observations of the 21-cm emission line. The color map has been binned in the same 10 colors used in Fig. 5 to outline velocity contours.

to be strong enough to affect the inner parts of this massive galaxy, where asymmetries must have a different origin.

One possibility that NGC 1365 is in the advanced stages of a minor merger. However, the absence of noticeable disturbance to the stellar bar requires that the infalling dwarf had a low enough density to have been tidally disrupted before reaching the bar region. Another possible explanation might be that a stream of gas has fallen in, perhaps from a tidally disrupted cloud or gas-rich dwarf galaxy. Such a stream, which would have to be more substantial than that detected in NGC 6946 (Kamphuis & Sancisi 1993; Boomsma *et al.* 2004) or the high-velocity clouds of the Milky Way (Wakker & van Woerden 1997), may have passed to the west of the center and ahead of the leading side of the bar. The ram pressure of this gas acting on the gas in the galaxy mid-plane might have removed a good

fraction of the upstream gas ahead of the original position of the shock, and allowing the shock to advance to its observed position. This scenario is not without its problems, however; most notably, the HI distribution is not noticeably depleted and the velocity pattern is not strongly disturbed where the gas stream is supposed to have punched through the mid-plane.

Whatever their origin, the peculiarities of the velocity field have proved a major obstacle to the objectives of this study.

4. Rotation Curve

We first determine the center, systemic velocity, position angle and inclination from the H α velocity map using the χ^2 minimization technique proposed by Barnes & Sellwood (2003). Their method uses the entire kinematic map (excluding the sparse gas in bar region), in order to estimate these projection parameters. We find that the center lies only a few arcsec from the reported position of the nucleus (Lindblad *et al.* 1996), and adopt their quoted position of the nucleus as the kinematic center for the rest of our analysis. The fitted inclination of 41° and PA of 220° agree well with the values obtained from the AIPS routine GAL, while the fitted heliocentric velocity of 1631.5 for the H α map and 1632 km/s for the HI map are in excellent agreement with the value of 1632 km/s reported by JvM95.

Applying a similar χ^2 minimization to the I-band image yielded the same PA but a higher inclination: $i = 52^\circ$, which is in tolerable agreement with the value $i = 55^\circ$ estimated by Lindblad (1978) also from photometric isophotes (see JvM95 and references therein). The large discrepancy between the kinematic and photometric inclinations is probably due to the strong spiral features that happen to lie near the projected major axis (see Palunas & Williams 2000; Barnes & Sellwood 2003). Since the spiral arms appear to bias the photometric inclination more, we adopt the kinematic inclination of $i = 41^\circ$, consistent with most other work. For completeness, we have also followed our analysis through using the photometric inclination, but find (§ 6.1) the kinematic inclination leads to superior fits.

In order to re-estimate the rotation curve from the HI velocity map, we excluded gas beyond a deprojected radius of $255''$ (23 kpc) from the center. Although the data extend $133''$ (12 kpc) farther, pronounced asymmetries in these outer parts suggest the gas layer is disturbed and may not be in simple rotational balance. While we cannot exclude the possibility that the gas layer in our selected inner region is warped, we here adopt the simpler assumption that the gas in the inner $255''$ is everywhere flowing in a single plane.

With the PA, inclination and systemic velocity fixed, we fitted for the circular velocity in annuli of 3 arcsec and 10 arcsec wide for the H α and HI data respectively. We fitted the

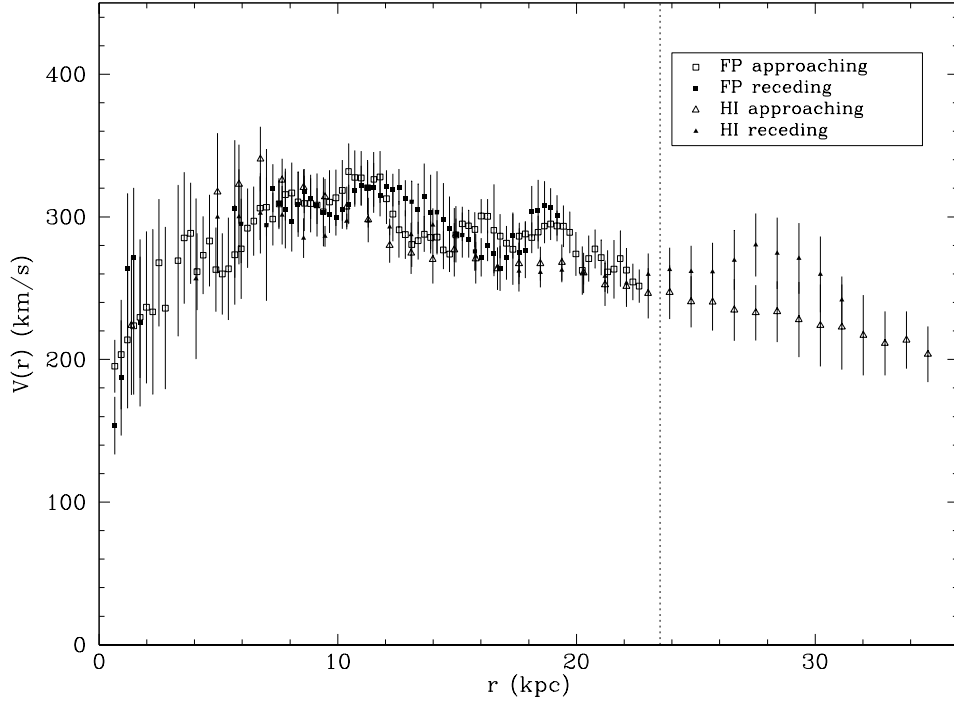


Fig. 8.— Rotation curve from 21-cm and $H\alpha$ observations. $V(r)$ was fitted for receding and approaching sides independently. Annuli for Fabry-Perot (FP) are 3 arcsec wide and HI map is 10 arcsec. Data outside $r=23.5$ kpc, marked by the vertical dotted line, has been ignored from our dark matter halo modeling.

approaching and receding sides separately, producing four separate estimates of the rotation curve, which we present in Fig. 8. Squares (triangles) represent fits to the Fabry-Perot (HI) observations, and we use open symbols for the approaching side of the galaxy and filled ones for the receding side. The uncertainties in the bar region are large because we here fit simple rotational motion to a flow pattern that is manifestly non-circular; we improve on this below. Fits with standard deviations greater than 60 km/s were discarded. In the inner disk, where we expect the galaxy to be flat, we find the four fitted velocities generally agree within the estimated uncertainties. However, there are substantial differences between the receding and approaching sides in the HI data beyond the vertical dotted line drawn at $R = 23$ kpc. Accordingly, we exclude data beyond 23 kpc (the region excluded for finding PA, inclination), for fitting our dark matter halo (§5.3).

The rotation speed declines significantly outside 10 kpc, although not as steeply as that derived by JvM95. A decline within the visible disk is not uncommon for galaxies of this luminosity (Casertano & van Gorkom 1991; Noordermeer *et al.* 2007).

5. Mass models

The first stage of our modeling procedure is to build a family of axisymmetric mass models with differing mass disks that, when combined with a halo, yield our adopted axisymmetric rotation curve, at least in the outer parts.

5.1. Disk

We compute the disk contribution to the central attraction by first assuming a fixed M/L ratio (Υ_I) for all the luminous matter, after rectifying the I-band image to face-on and applying a global correction for extinction. We used the inclination and PA obtained from the kinematic maps to perform the deprojection.

A constant Υ_I is a good assumption provided that the stellar population is homogeneous and dust obscuration is negligible. Most variations in the V-I color visible in Fig. 2 appear to be due to dust, which affects the V-band surface brightness much more than the I-band. While Fig. 1 shows that dust still diminishes the I-band surface brightness, especially in the bar region, we have not attempted to correct for the patchiness of the dust.

As we need the in-plane forces for both the strongly non-axisymmetric light distribution, and for an azimuthally averaged light profile, we adopt the same numerical procedure for both. We assume a finite thickness for the disk with the usual mass profile normal to the plane of the galaxy: $\rho(z) \propto \text{sech}^2(z/2h_z)$ with $h_z = 0.5$ kpc consistent with observations of edge-on galaxies for our measured disk scale length $r_d = 6.5$ kpc (Kregel, van der Kruit & de Grijs 2002).

Forces from the visible matter scale linearly with the adopted M/L ratio; we explore a discrete set of values for Υ_I ranging from 0.50 to 3.75 in steps of 0.25. Axisymmetric rotation curves from the visible matter for three different Υ_I values are shown by the solid lines in Fig. 9.

We have not explicitly determined the contributions from the mass of the neutral and molecular gas to the rotation curve. Most of the neutral gas, $\sim 1.7 \times 10^{10} M_\odot$ after helium correction, is outside the bar whereas all the molecular gas is inside the bar and nucleus, $\sim 1.7 \times 10^{10} M_\odot$ of which $5.4 \times 10^9 M_\odot$ lies in the central 2.0 kpc (see Sandqvist *et al.* 1995). Altogether gas accounts for about 10% of the total mass, as measured from the HI rotation curve (JvM95). The combined distribution of the two phases has a density profile that resembles that of the light and therefore can be taken into account by simply associating the stellar mass-to-light ratio to be roughly 90% of the fitted value. While this approximation

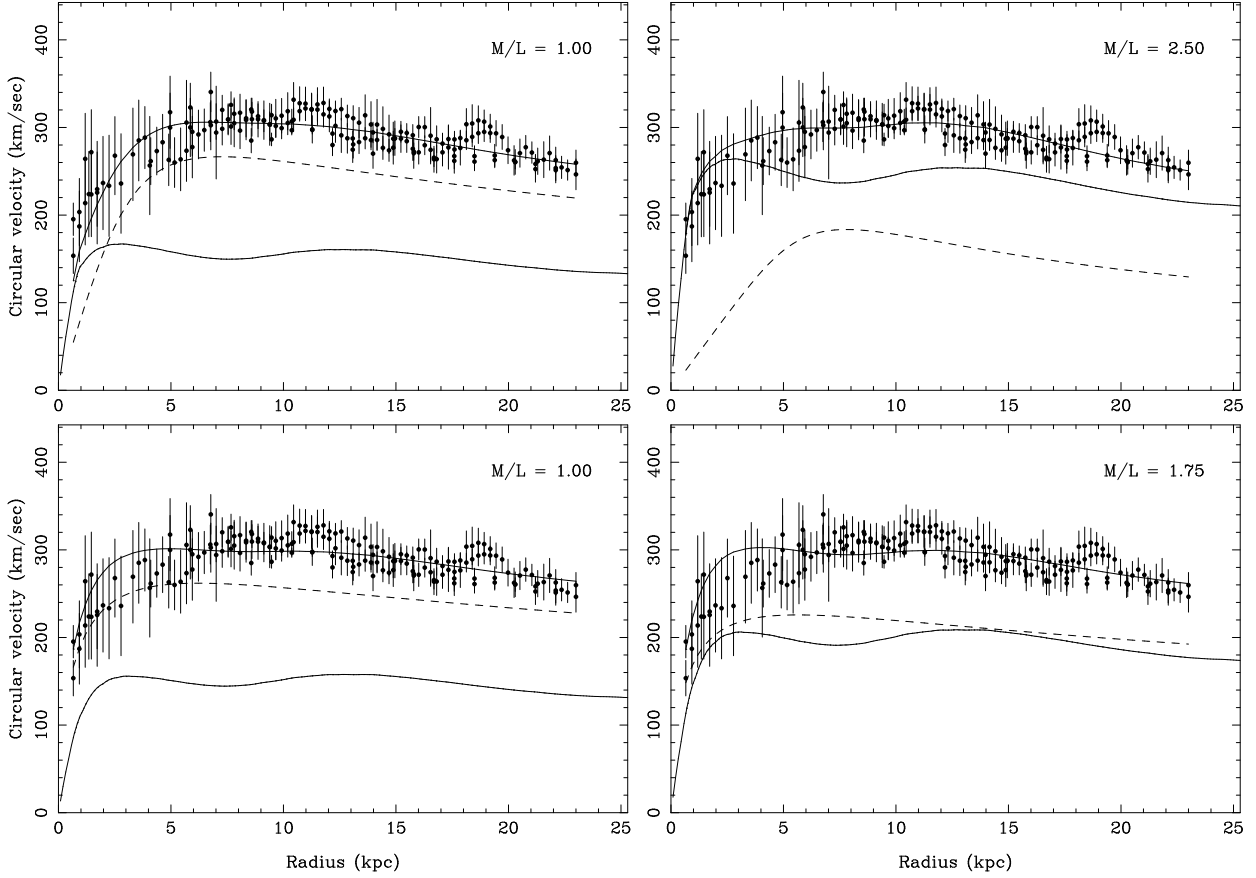


Fig. 9.— Mass models for the rotation curve. *Points and error bars*: Observed rotation curve in both HI and H α . *Uppermost solid line*: Best-fit total rotation curve. *Dotted line*: Contribution of the best-fit halo. *Lower solid line*: Contribution of the stellar disk to the total rotation curve. The left panels have disk $\Upsilon_I = 1.0$ and the right panels have disk $\Upsilon_I = 2.50$ and $\Upsilon_I = 1.75$. The top panel use pseudo-isothermal halos with bulge b1075. Bottom panels use NFW halos.

neglects the different thicknesses of the star and gas layers, the total rotation curve will be very little affected by taking into account the marginally stronger central attraction from the small fraction of mass in the gas.

5.2. Bulge

The assumptions of constant Υ_I and disk thickness at all radii are clearly the simplest we could adopt, but may not be correct, especially in the center. While the light distribution in the inner bar region is somewhat rounder than that in the outer bar, it does not really suggest a spheroidal bulge because deprojection, which stretches the image along the minor

axis, still leaves this component roughly aligned with the bar. However, it is possible that the inner bulge-like feature is thicker than the disk and bar and it may also have a higher Υ_I than the rest of the disk.

To allow for a possible enhanced Υ in the inner disk, we consider some simple variants of our constant Υ_I models. For $r \leq r_b$, we scale the Υ_I by the function

$$F(r) = 1 + f \times \left(1 - \frac{r}{r_b}\right) \left(1 + \frac{r}{r_b}\right)^2, \quad (1)$$

where r_b is the radius of the bulge and f is a constant. We have adopted three separate values of r_b and of f , and label the five bulge models we study here as b1025, b1075, b2050, b2075, b3075. The first numerical digit denotes r_b in kpc and the last 3 digits are 100 times the value of f ; *i.e.* b2050 denotes a model bulge with $r_b = 2$ kpc and $f = 0.50$.

This approach assumes that the possible bulge is as thin as the outer disk, which may not be true. A thicker component would exert slightly weaker central forces, which will result in our fits preferring a slightly lower value of f than the population has in reality. However, we do not need to know the relative flattening of this mass component; our procedure simply allows for the possibility that it may give rise to some extra central attraction.

As found by Jungwiert, Combes & Axon (1997) for their H-band image, the inner light profile of our I-band image is extended at different position angle from that of the main bar. Jungwiert *et al.* and Laine *et al.* (2002) suggest this is evidence of decoupled nuclear bar although an HST NICMOS image resolves this feature into a nuclear spiral (Emsellem *et al.* 2001; Erwin 2004). Whatever the correct interpretation, this distortion in the inner light distribution is inside the region we exclude from our fits to the observed velocities, and does not affect our conclusions.

5.3. Halo

The total central attraction should account for the rotational balance, and generally requires a dark halo. We have adopted 2 different dark halo forms: a generalized pseudo-isothermal halo and the NFW density profile (Navarro *et al.* 1997).

In order to fit the declining rotation curve, we adopt a slightly generalized pseudo-isothermal dark matter halo density profile of the form proposed by van Albada *et al.* (1985):

$$\rho(r) = \rho_o \frac{1}{1 + (r/r_c)^k}. \quad (2)$$

The exponent k is treated as an independent parameter that allows the halo circular speed to decline if $k > 2$. Since large values of k lead to a halo rotation curve with a sharp, narrow peak, we apply the additional constraint $k \leq 5$.

NFW (Navarro *et al.* 1997) dark halo profiles have the form

$$\rho(r) = \frac{\rho_s r_s^3}{r(r + r_s)^2}. \quad (3)$$

For both density profiles we fit the total rotation curve by minimizing χ^2 to find the best fit halo to be combined with each adopted disk Υ_I and bulge model. The results are given in Table 1 and Table 2, with the values of c and V_{200} being computed for a Hubble constant $H_0 = 70 \text{ km s}^{-1} \text{ Mpc}^{-1}$. No bulge modification was applied to the NFW halo since extra bulge mass combined with the cuspy halo would have complicated the fits to the inner rotation curve. Figure 9 shows possible fits to the data with different Υ_I exemplifying the disk-halo degeneracy for both dark matter halo profiles adopted. The pseudo-isothermal profile plotted uses a bulge model b1075.

Both our adopted halo functions assume spherical symmetry, whereas we need assume only that the halo is axisymmetric in the disk plane. The flow pattern in our simulations depends on Υ_I and the corresponding halo attraction; the possible flattening of the halo affects only the interpretation of the halo attraction in terms of a mass profile. As a flattened halo gives rise to stronger central attraction in the mid-plane for the same interior mass (*e.g.* Fig. 2-12 Binney & Tremaine 1987), the simplest assumption of spherical symmetry allows a more massive halo than would be required if the halo were significantly oblate.

6. Gas Dynamics simulations

We here give a brief summary of our procedure; see Weiner *et al.* (2001) for a more detailed description. As usual, we neglect self-gravity of the gas, which would add considerably to the computational complexity of our many simulations. This simplifying assumption is justified because the gas density in the bar, where we are most interested in comparing with the observed velocities, is a small fraction of the mass in stars.

We compute the gas flow using the flux splitting code written and tested by van Albada (1985) and kindly provided by Athanassoula. Pérez (2007) has shown that results from the 2-D code we use and the 3-D SPH code used in her work agree very well for the same mass model, which is reassuring.

Since the I-band light has excellent 2-fold rotation symmetry (Fig. 1), we force bi-

symmetry in the simulations and employ an active grid covering only one half of the galaxy. In order to avoid initial transients resulting from non-equilibrium starting conditions, we begin our simulations in an axisymmetric potential, and gradually change to the full non-axisymmetric barred potential over the first 2.5 Gyr of evolution. Careful inspection of the simulations revealed that the gas does not settle to a quasi-steady flow until several bar rotations (3 Gyr or from 6 to 15 rotations for $\Omega_p = 12$ and 32 respectively) are completed. At this time, we take a snapshot of the simulation and compare it to the data. We stress that the final state of the gas doesn't depend on the growing time, but the bar growth rate does affect how quickly the gas flow settles down.

We experimented with different sound speeds and grid resolutions, which generally yielded reproducible results except in the central few resolution elements. We found that flows at the highest resolution (grid cell size 128 pc) did not ever settle to quasi-steady patterns for the most massive disks, but did do so for a cell size of 300 pc; this change in behavior is caused by the stabilizing influence of greater numerical viscosity on the coarser grid. We therefore work with the results from simulations with a grid cell size of 300 pc for all disk masses.

Modeling the ISM with a simple fluid code is clearly an approximation. An isothermal equation of state with sound speeds in the range 6 to 10 km s⁻¹ is reasonably appropriate for the warm neutral and warm ionized components, which have temperatures of $\sim 10^4$ K, and we attempt to fit our models to the observed kinematics of the ionized component. The neutral HI component of the Milky Way (Gunn, Knapp & Tremaine 1979) and other galaxies (*e.g.* Kamphuis 1993) is also observed to have intrinsic line widths in this range. Furthermore, dense clouds are observed also to maintain a velocity dispersion of ~ 8 km s⁻¹ (Stark & Brand 1989). Englmaier & Gerhard (1997) showed that the gas flow pattern in their simulations changed materially when they increased the sound speed to 25 km s⁻¹; however, such a large sound speed is not representative of any dynamically significant component of the ISM. We therefore confine our tests of the gas parameters to realistic ranges, and find the significant properties of the flow are almost independent of the exact values adopted.

The non-circular flow pattern produced by a bar depends both on the mass of the bar and its pattern speed or rotation rate (Roberts *et al.* 1979). For the photometric disk model described above, the bar mass scales directly with the adopted Υ_I , while the total central attraction includes the contribution from the adopted halo, which is assumed to be axisymmetric. For each adopted Υ_I ratio, we compute the gas flow in the disk plane using 2-D gas dynamics simulations, for a number of different bar pattern speeds, Ω_p . We project the resulting flow patterns as the galaxy is observed, and compare with Fabry-Perot velocity

maps using a χ^2 analysis to find the best match to the observations, in order to estimate the disk Υ_I and Ω_p .

We explored pattern speeds in the range $12 \leq \Omega_p \leq 32 \text{ km s}^{-1} \text{ kpc}^{-1}$, corresponding to corotation radii in the range $2.0r_B \gtrsim r_L \gtrsim 0.9r_B$. In all we ran 154 simulations to cover the grid in Ω_p and Υ_I for each of the pseudo-isothermal and NFW halo models.

6.1. Comparison between models and data

Before attempting any comparison between simulations and data, it is necessary to smooth the simulations to the atmospheric seeing during the observations and also by the largest kernel used to produce the velocity map (see §2.2), which requires a smoothing kernel of $\text{FWHM} = 4''$. Kamphuis (1993) reports that the velocity dispersion of HI gas rises inwardly for a number of galaxies to values that exceed 10 km s^{-1} in the bright inner parts of massive galaxies. Since the velocity in each pixel may reflect that of an individual HII region, we add 12 km s^{-1} in quadrature to the formal error estimates of the $\text{H}\alpha$ velocities to allow for a possible peculiar velocity relative to the mean flow.

Since our simulations assume a gas with a finite sound speed, the full non-linear velocity distribution at every point takes into account our adopted velocity spread. No further correction, *e.g.* for asymmetric drift, is therefore needed.

We compare the projected snapshot from the simulation using the standard goodness of fit estimator

$$\chi^2 = \frac{1}{N} \sum_{i=1}^N z_i^2, \quad (4)$$

where the summation is over all N pixels in the region selected for comparison, and z_i is the usual difference between the observed velocity $V_{i,\text{obs}}$ and that predicted from the simulation $V_{i,\text{mod}}$, weighted by the uncertainty σ_i ; viz.

$$z_i = \frac{V_{i,\text{obs}} - V_{i,\text{mod}}}{\sigma_i}. \quad (5)$$

We include 2280 pixels in the fit, but they are not all independent because of seeing and smoothing. Furthermore, the quantity χ^2 is regularized somewhat by adding 12 km s^{-1} in quadrature to the errors. Thus it is not a formal estimator of confidence intervals, but can be used to compare relative goodness of fit.

Our mass model is bi-symmetric, in line with the light in this galaxy, but the velocity

data are not. Our simulations are therefore unable to fit both sides of the bar simultaneously.⁴ Since the dust lane and steep velocity gradients are quite uncharacteristically almost outside the bar on the west side, we confine our fits to the east side, where we suspect that the flow pattern is less disturbed.

We further restrict the region from which we evaluate χ^2 to only those pixels in the area between the inner ellipse and the outer rounded rectangle shown in Fig. 5, because our models are most sensitive to the parameters we have varied in this region. The inner ellipse has a semimajor axis of $35''$ and ellipticity 0.5, while the semi-axes of the outer curve are $80''$ & $42''$. We exclude the center for several reasons: the observed velocities are degraded somewhat by beam smearing, our assumptions of a thin disk are most likely violated in the center (see section 5.2), and the predicted gas velocities vary with grid resolution in this region. We exclude data in the spiral arms because the gas flow outside the bar never settles to a steady pattern in our simulations, and some studies (*e.g.* Sellwood & Sparke 1988) suggest that these features evolve over time.

The value of χ^2 varies substantially as the two parameters are varied, but the minimum remains large, even when we restrict the region of comparison with the data to the eastern half of the bar. Maps of the residuals, shown below, reveal a number of isolated regions with substantially discrepant velocities that coincide with the regions labeled in Fig. 5. In order to check whether the position of the minimum was being displaced by the pixels with large anomalous velocities, we employed Tukey’s biweight estimator (Press *et al.* 1992)

$$\chi_{\text{bw}}^2 = \frac{1}{N} \sum_i \begin{cases} z_i^2 - z_i^4/c^2 + z_i^6/(3c^4) & |z_i| < c, \\ c^2/3 & \text{otherwise,} \end{cases} \quad (6)$$

with the recommended value for the constant $c = 6$. In fact, the position remained unchanged for both the isothermal and NFW halos, and we revert for the remainder of the paper to the usual χ^2 statistic defined by eq. (4).

The minimum of the reduced χ^2 is unreasonably high: $\chi^2 = 2.7$ for the best isothermal halo and $\chi^2 = 2.4$ for the NFW halo. It is evident from the residual maps (Figure 10a & b) that a large part of the mismatch from the model comes from the five anomalous regions identified already in Fig. 5. We therefore masked each of these regions with circular mask of radius 4 or 5 pixels, which decreased the minimum of χ^2 to 1.6 for the isothermal models and 1.5 for then NFW halo models. While these values are still on the high side, we should not expect $\chi^2 = 1$ since the fluid model is idealized. We therefore consider we have satisfactory models for most of the flow pattern in the eastern half of the bar.

⁴Since the I-band light distribution is almost perfectly bisymmetric (Fig. 1), relaxing the assumption of bi-symmetry had a negligible effect on the model predictions.

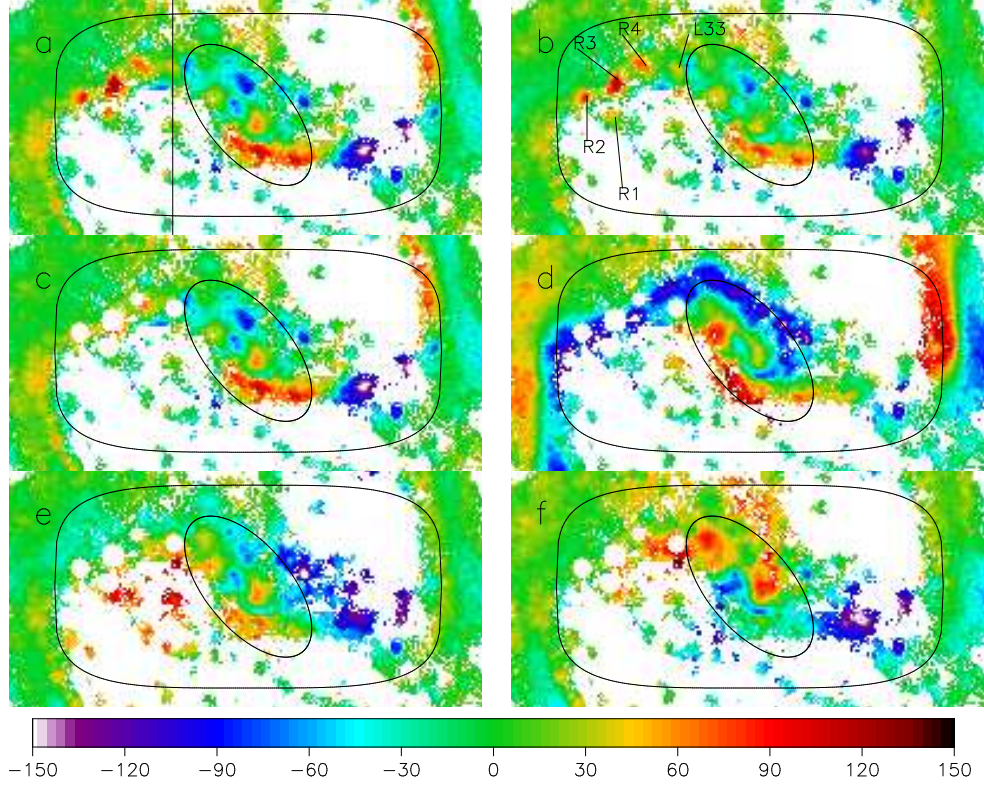


Fig. 10.— (a) & (b) Residual maps for respectively the best-fit pseudo-isothermal and NFW halo models. The velocities of the anomalous HII regions, identified in (b), are shown in these two panels only. The N-S line in (a) is described in §6.3. (c)-(f) 4 characteristic b1075 models, with the anomalous HII regions masked out: *c.*) $\Upsilon_I = 2.50$, $\Omega_p = 24$; *d.*) 1.0, 24; *e.*) 2.50, 16; *f.*) 1.0, 16.

Since we approximate the ISM as an isothermal gas, the shock in the simulations must be as close as the code can resolve to a discontinuity, whereas it is possible that gas velocities in NGC 1365 vary more gradually. We therefore experimented with additional smoothing of the simulations above the $\text{FWHM} = 4''$ that matches the resolution of our data. The value of χ^2 decreases considerably to $\chi^2 = 1.3$ when we smooth the simulations by $10''$, although the position of the minimum did not change. At least some of this improvement appears to result from a better match to the velocity gradient across the shock. We have not included this extra smoothing in the fits below, however, because it degrades our resolution everywhere and reduces the curvature of the χ^2 surface.

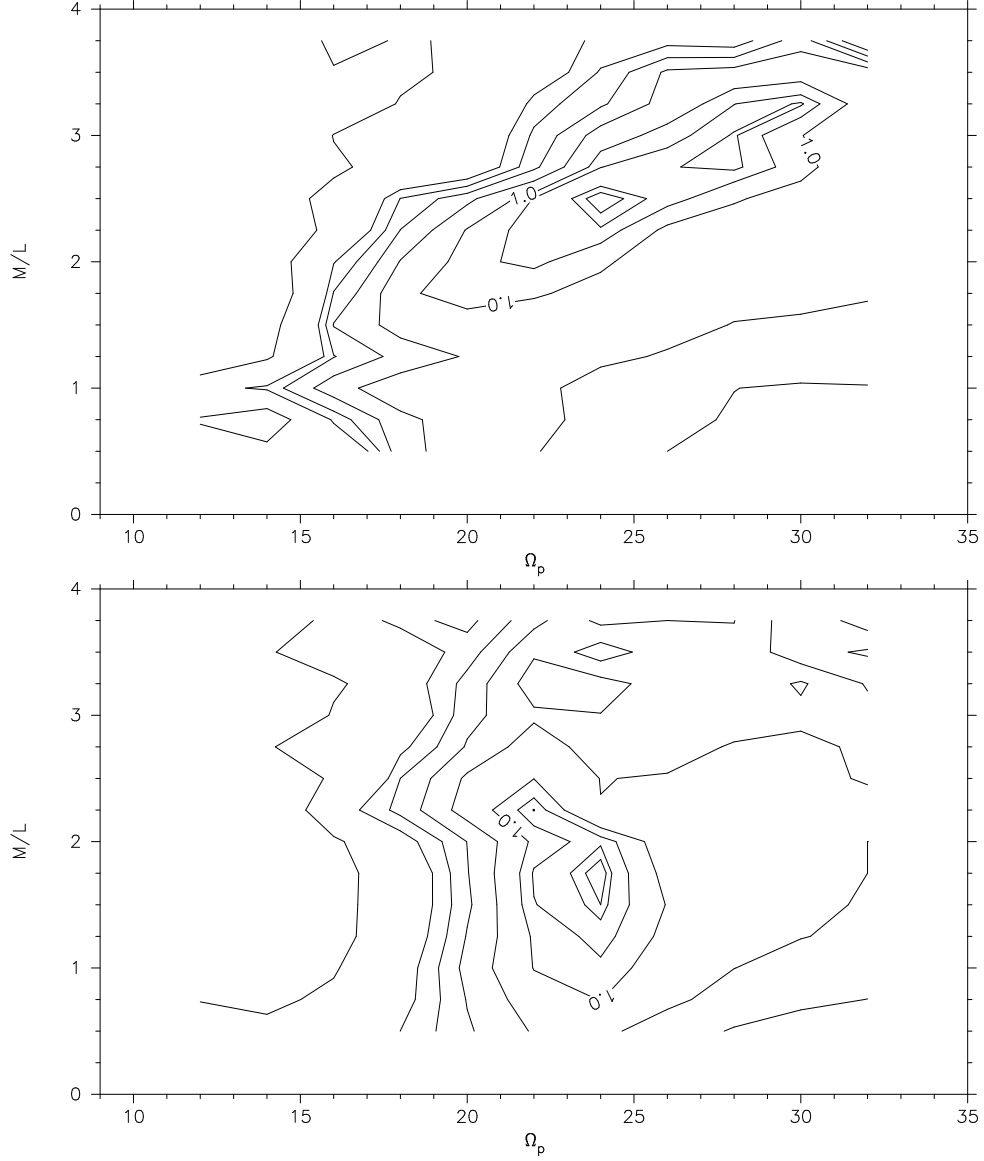


Fig. 11.— *Upper*: The χ^2 surface for the b1075 pseudo-isothermal model. The minimum value (1.6) lies at $\Upsilon_I = 2.50$ and $\Omega_p = 24$. Contours are drawn at $\Delta\chi^2/N$ 0.1, 0.2, 0.5, 1, 2, 3, 4, 5 & 10 above the minimum. *Lower*: The same for the NFW halo model. The minimum is 1.5 for model with $\Upsilon_I = 1.75$ and $\Omega_p = 24$.

6.2. Best fit models

Figure 11 shows contours of χ^2 in the space of the two principal parameters: Υ_I & Ω_p . The quantity contoured is the value from eq. (4) using pixels from the east side of the bar only with the 5 anomalous regions masked out.

For the pseudo-isothermal halos, models with low pattern speed and high Υ_I are very

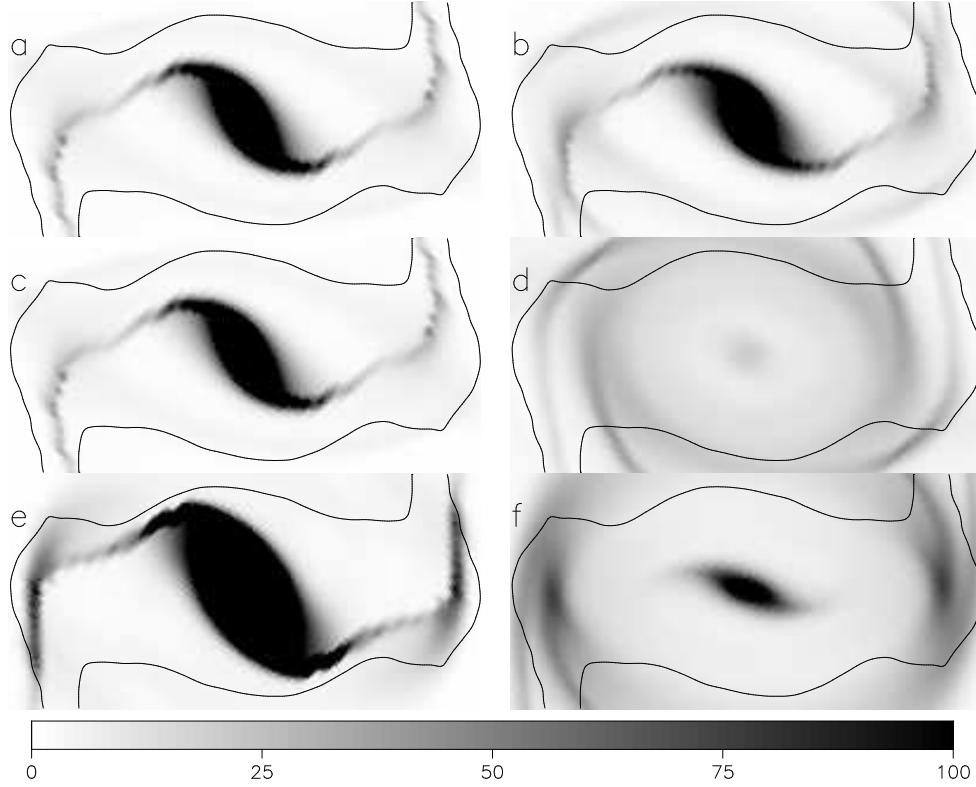


Fig. 12.— Gas surface density in the same models shown in Fig. 10, panels (a) & (c) are identical, therefore. Panels (c) thru (f) show that the density response to bar forcing changes dramatically as the disk mass and pattern speed are varied.

strongly disfavored and the χ^2 function also rises strongly, but somewhat less steeply towards higher pattern speeds and low Υ_I . We show the residual map for the best fit parameters and, for comparison, three other cases for two different values of Ω_p and Υ_I in Figure 10(c)-(f).

Figure 12 shows the gas density response in the inner regions of the same set of models. Shocks are regions of locally high gas density along the bar that coincide with steep velocity gradients in the flow. The shocks in the best fit models (top row) are displaced towards the leading edge of the bar, as usual, and all-but disappear in the low-mass disks, panels (d) & (f). The shocks in panel (e) are too far towards the bar’s leading edge, and the inner oval is too large, because the x_2 family that is responsible for this behavior (Sellwood & Wilkinson 1993) grows in spatial extent as the pattern speed is reduced. Although the position of the dust lane in the west of the bar is indeed shifted towards the leading edge, it does not have the shape predicted by low pattern speed models.

It is difficult make a more quantitative comparison between the gas density in the models and that observed. We do not have sufficient information about the distribution of all the

multiphase components of the ISM; we do not have a complete CO map, and the spatial resolution of the HI map from the VLA is too low to attempt a meaningful fit.

The best fit pattern speed for both the pseudo-isothermal and NFW halos is for $\Omega_p = 24 \text{ km s}^{-1} \text{ kpc}^{-1}$ which places corotation at $r_L \approx 1.23 r_B$. This value of Ω_p is in good agreement with that obtained by Lindblad, Lindblad & Athanassoula (1996) in their bar-only model (after correcting their assumed distance to ours).

However, the minimum χ^2 is at $\Upsilon_I = 2.50$ for the pseudo-isothermal halos, whereas the somewhat lower value $\Upsilon_I = 1.75$ is preferred for NFW halo models. The rotation curve decompositions for these two models are shown in the right hand panels of Fig. 9. An estimate of the statistical uncertainty in the parameters is indicated by the $\Delta\chi^2 = 1$ contour in Fig. 11. Both results are in agreement with each other within the uncertainties and favor fast bars and moderately massive disks.

Finally, we reworked our entire analysis using the photometric inclination of $i = 52^\circ$ instead of the conventionally adopted kinematic inclination of $i = 41^\circ$ in the foregoing analysis. This required redetermining the gravitational potential of the differently oriented and projected bar and disk, refitting for the halo parameters for each adopted Υ_I , and running a new grid of models over the two free parameters. The resulting fits were far worse, with the minimum value of $\chi^2 \simeq 3.8$, even after masking out the HII regions having anomalous velocities. This test confirms that the kinematically-determined inclination is the more appropriate.

6.3. Pseudo-slit cut through data

Shocks across dust lanes are readily identified as steep velocity gradients. The data points in Figs. 13 and 14 show the observed velocities along a pseudo-slit placed perpendicular to the bar major axis as shown in Fig. 10(a); this cut across the bar has the most extensive data. The lower panel shows the V-I color along the same line, which reveals that the projected velocity gradient of almost 200 km s^{-1} is coincident with the prominent dust lane. The vertical dotted lines mark the bar width as presented in the bar isophote in Figs. 1 and 2. The other lines in the upper panel show velocities from our b1075 isothermal simulations for different Υ_I with a fixed $\Omega_p = 24 \text{ km s}^{-1} \text{ kpc}^{-1}$ (Fig. 13) and for different Ω_p for a fixed $\Upsilon_I = 2.50$ (Fig. 14).

These figures show that $\Upsilon_I = 1$ does not produce a strong enough shock, and $\Omega_p \neq 24$ puts the shock/velocity gradient in the wrong place. In fact, the systematic dependences of the velocity gradient on Υ and on Ω_p are quite similar to those shown in the pseudo-slits for

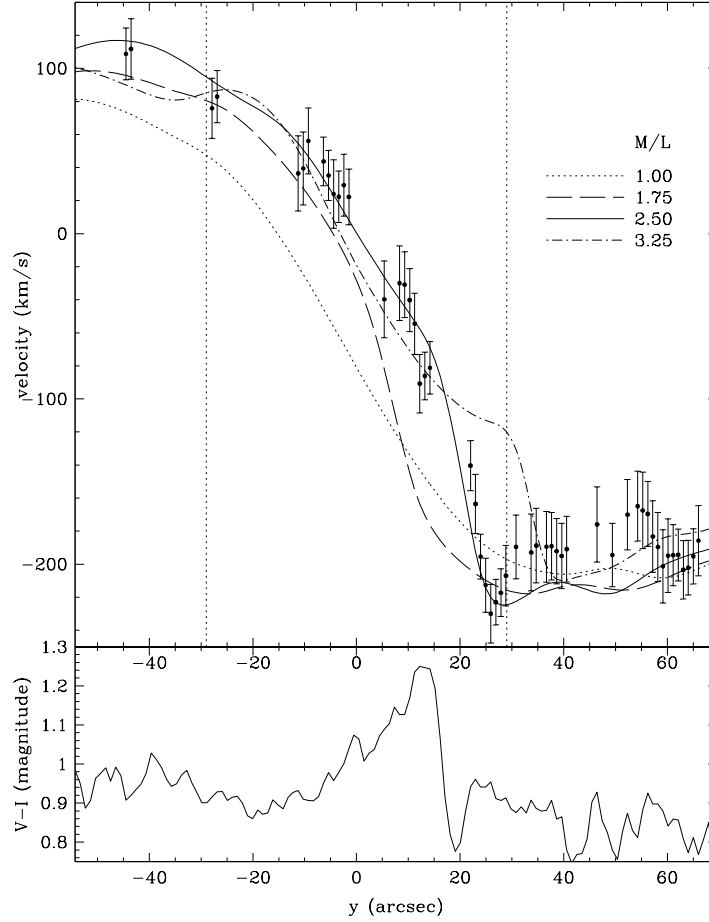


Fig. 13.— Data points with error bars show the $H\alpha$ velocities along a pseudoslit passing perpendicular through the bar as indicated in Fig. 10(a). The two vertical dotted lines mark the width of the bar. Different curves show the simulated velocities in models with different Υ_I ratios for $\Omega_p = 24$ and the b1075 model. Lower panel shows the color profile along the same pseudoslit through our extinction map (Fig. 2).

NGC 4123 (Weiner *et al.* 2001), where the effects of these physical parameters are explained.

7. Discussion

In the previous section, we argued that the underlying gas flow in the eastern half of the bar can be modeled with a somewhat massive disk embedded in one of two different halos. Neither model makes a compelling fit, however, and the properties of both best-fit halo models are distinctly non-standard. The outer profile of both our fitted dark halo

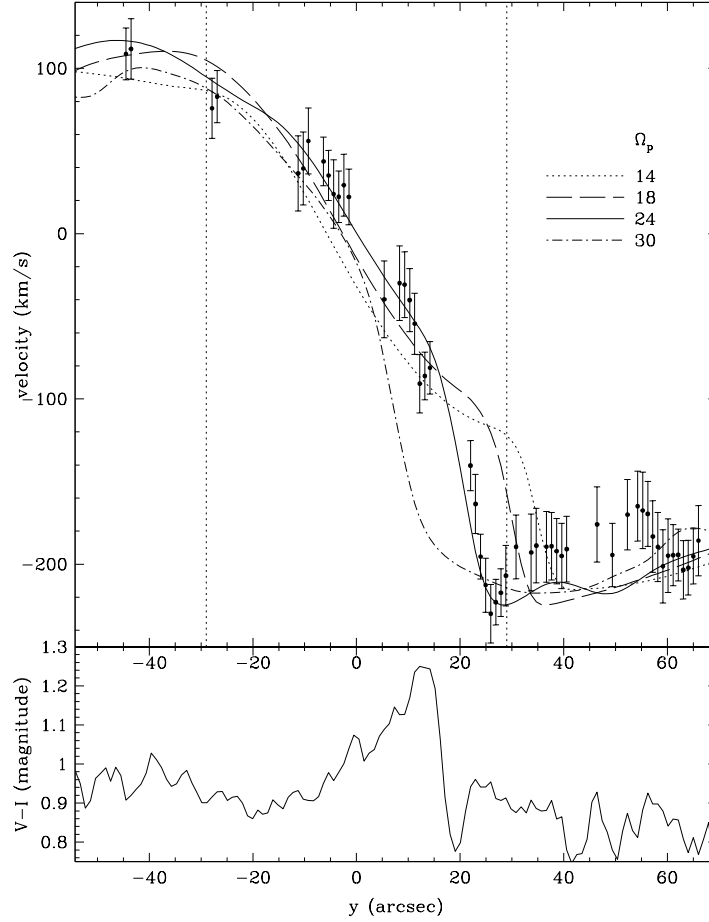


Fig. 14.— As for Fig. 14 but here the curves show simulations having different Ω_p for fixed $\Upsilon_I = 2.50$.

models already yields a declining circular speed by the edge of the visible disk. This finding may simply be a reflection of a mis-estimated rotation curve, possibly due to a warp or tidal disturbance. However, in their attempt to fit a warp, JvM95 obtained a more strongly declining rotation curve, which would require a still less orthodox halo model.

7.1. Disk mass

Our principal finding is that the bar must be massive and rapidly rotating in order for the underlying gas flow pattern to resemble that observed. We obtain improved fits with the isothermal model when we increase the baryonic mass in the inner (bulge-like) region

and also when we adopt a halo function that has a high density near the center. This fact suggests that the flow pattern requires a high density in the center, but cannot determine whether the mass should be flattened or spherical, baryonic or dark.

7.2. Dynamical friction

The disk contribution to the central attraction in our best fit model with the NFW halo function, though large, is not fully maximal (Fig. 9), yet the bar is required to be fast. This model therefore presents the additional puzzle that dynamical friction (Debattista & Sellwood 2000) has not slowed the bar. The uncertainty in Υ_I is great enough that more massive disks are acceptable, although such models would further increase the uncomfortably high ratio of baryonic to dark mass of the best fit model. A lower value of Υ_I may allow a more reasonable baryonic fraction, but exacerbates the puzzle of the fast bar in a yet denser halo.

7.3. Halo decompression

The halo of our best-fit NFW model has $V_{200} = 111 \text{ km s}^{-1}$ and a concentration $c = 61$. These parameters, which are defined in Navarro *et al.* (1997), are not in line with the predictions of LCDM theory (*e.g.* Bullock *et al.* 2001); the concentration is very high and the value of V_{200} much lower than expected for a large galaxy.

However, these fitted parameters are for the current halo of NGC 1365, which must have been compressed as the massive disk formed. We have therefore adopted the procedure described by Sellwood & McGaugh (2005) to try to determine the parameters of the original uncompressed halo before the disk formed. The value $\Upsilon_I = 1.75$ for our best fit model yields a disk mass $M_d = 1.6 \times 10^{11} \text{ M}_\odot$, which must have condensed from the original uncompressed halo to its present radial distribution. Assuming the dark matter in the original halo to have an isotropic velocity distribution, we determine the final mass profile of the dark matter from some assumed initial NFW form. We proceed by trial and error to determine the initial halo that yields a final rotation curve that closely resembles the fit shown in right-bottom panel of Fig. 9 for $\Upsilon_I = 1.75$

We find that an initial NFW halo with the properties $c = 22$, $V_{200} = 123 \text{ km s}^{-1}$, $M_{200} = 5.9 \times 10^{11} \text{ M}_\odot$, and $r_s = 8 \text{ kpc}$ resembles the mass model of the final best-fit NFW halo, as shown in Figure 15. The inner halo is an excellent match, but the density of the compressed halo is fractionally higher than in Fig. 9 beyond $r = 10 \text{ kpc}$, which we tolerate because it errs on the side of allowing a more massive halo. Nevertheless, the concentration

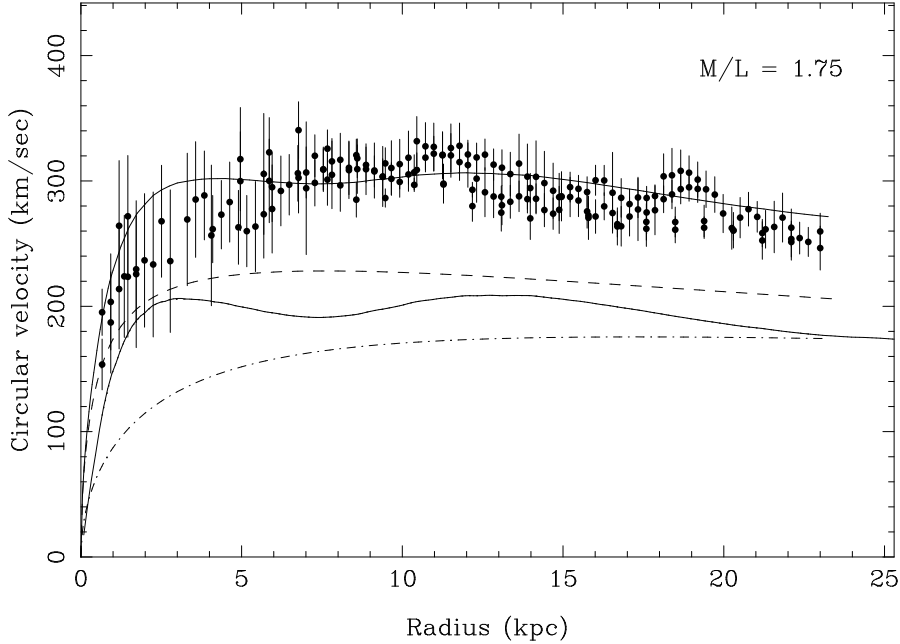


Fig. 15.— Rotation curve of the compressed NFW halo model. The dot-dash line shows the uncompressed halo, the dashed line shows the halo after compression, while the other two lines show the disk contribution and the total rotation curve.

is still high, though less extreme than if compression is neglected, and V_{200} is still low for such a massive galaxy. Furthermore the disk mass fraction, $M_d/M_{200} \simeq 0.27$ is much greater than the expected value of ~ 0.05 (e.g. Dutton *et al.* 2007). Since our estimated value even exceeds the cosmic dark matter fraction (Spergel *et al.* 2007), it may indicate an unusual formation history for this galaxy.

7.4. Population synthesis models

In this study, we have obtained a dynamical estimate of Υ_I for NGC 1365. In previous work, we obtained estimates by the same procedure for NGC 4123 (Weiner *et al.* 2001) and NGC 3095 (Weiner 2004). Here we compare our estimated values of Υ_I with the predictions from population synthesis models by Bell *et al.* (2003) for a galaxy of the observed B-V color. Since Bell *et al.* (2003) do not give predictions for our measured V-I color index, we also compare with the earlier predictions of Bell & de Jong (2001).

Table 3 presents the comparison for all three galaxies. We give isophotal magnitudes corrected for internal (Giovanelli *et al.* 1994; Sakai *et al.* 2000) and foreground extinction (Schlegel, Finkbiner & Davis 1998), and determine the predicted Υ_I from the B-V color

using table 7 of Bell *et al.* (2003), and from the V-I color using table 1 of Bell & de Jong (2001). Bell *et al.* (2003) suggest the uncertainty in their prediction is 0.1 dex, or some 25%. The final column gives our dynamically-estimated value of Υ_I for each of the three galaxies.

Our dynamical estimates of $\Upsilon_I \simeq 2 - 2.25$ agree reasonably well with the values of 1.5 – 2.1 deduced from the stellar population V-I colors for a “diet Salpeter” IMF Bell & de Jong (2001). However, our dynamical modeling estimates are higher than those inferred from B-V colors Bell *et al.* (2003), suggesting that these galaxies are somewhat bluer in B-V for a given V-I than are the stellar population models; B-V is more sensitive than V-I to the details of recent star formation.

Our fluid dynamical Υ_I values provide a zeropoint normalization for the stellar population models that is at or slightly higher than the preferred normalization of de Jong & Bell (2007). The present work makes this conclusion firmer by removing some distance uncertainty in Υ , since NGC 1365 has a Cepheid distance while NGC 3095 and NGC 4123 do not. The Υ_I values from dynamics make it difficult to have a very low disk, $\Upsilon_I \lesssim 1.0$, as advocated by some authors to reconcile the Tully-Fisher relation zeropoint or lack of radius dependence with theoretical expectations (Portinari, Sommer-Larsen & Tantaló 2004; Pizagno *et al.* 2005).

8. Conclusions

We have presented a detailed study of the strongly-barred galaxy NGC 1365, including new photometric images and Fabry-Perot spectroscopy, as well as a detailed re-analysis of the neutral hydrogen observations by Jörsäter & van Moorsel (1995). We find the galaxy to be at once both remarkably bi-symmetric in its I-band light distribution and strongly asymmetric in the distribution of dust and gas, and in the kinematics of the gas. These asymmetries extend throughout the galaxy, affecting the bar region, the distribution of gas in the spiral arms and the neutral hydrogen beyond the edge of the bright disk. The velocity field mapped in the H α line showed bright HII regions with velocities that differed by up to $\sim 80 \text{ km s}^{-1}$ from that of the surrounding gas. Our sparsely-sampled line profiles in these anomalous velocity regions hint at unresolved substructure, suggesting a possible double line profile.

The strong bar and spiral arms complicate the determination of the projection geometry of the disk, assuming it can be characterized as flat in the inner parts. The inclination of the plane we derive from the kinematic data is smaller by about 10° from that determined from the photometry. The strong spiral arms that cross the projected major axis far out in the

disk seem likely to bias the photometric inclination and we therefore adopt, in common with other workers, the inclination derived from the gas kinematics. This preference is supported by the much poorer fits to the observed kinematics obtained when we adopt the photometric inclination (§ 6.1).

Our attempts to derive the rotation curve of NGC 1365 were complicated by the fact that neither the $H\alpha$ nor the HI velocity maps are consistent with a simple circular flow pattern over a significant radial range. The bar and spirals clearly distort the gas flow in the luminous disk. The neutral hydrogen extends somewhat beyond the visible disk but unfortunately has neither a uniform distribution nor regular kinematics. JvM95 attempted to fit a warp to the outer HI layer that extends into the visible disk, and derived a strongly declining rotation curve. We chose instead to assume a coplanar flow out to a deprojected radius of $255''$ and to neglect the asymmetric velocities in the neutral hydrogen beyond. The velocities derived separately from the $H\alpha$ and HI data are in good agreement. Our resulting rotation curve shows a gentle decrease beyond a radius of ~ 10 kpc, similar to those observed in other massive galaxies (Casertano & van Gorkom 1991; Noordermeer *et al.* 2007).

We used our deprojected I-band image to estimate the gravitational field of the luminous matter, which can be scaled by a single mass-to-light ratio, Υ_I . We also employed a gradual increase to Υ_I in the central few kpc to allow for an older bulge-like stellar population, although the light distribution does not appear to have a substantially greater thickness near the center. We combined the central attraction of the axially-symmetrized disk for various values of Υ_I with two different halo models to fit the observed rotation curve in the region outside the bar – finding, as always, no significant preference for any Υ_I .

We attempt to fit hydrodynamic simulations of the gas flow pattern in the bar region, in order to constrain Υ_I . For each type of halo adopted, we run a grid of simulations covering a range of both Υ_I and Ω_p , the pattern speed of the bar. We then project each simulation to our adopted orientation of the galaxy and compare the gas flow velocities in the model with those observed. Since the light distribution in NGC 1365 is highly symmetric, our simulations were constrained to be bi-symmetric, yet the observed gas flow has strong asymmetries. None of our simulations is capable, therefore, of fitting both sides of the bar simultaneously.

The anomalous position of the dust lane in the western part of the bar suggests that side is the more likely to be disturbed, and we therefore fit our models to the eastern half of the bar only. After smoothing the model to match the resolution of the kinematic data and masking out five blobs of gas with strongly anomalous velocities, we are able to obtain moderately satisfactory fits to the remaining velocities. The best fit pattern speed is $\Omega_p = 24 \text{ km s}^{-1} \text{ kpc}^{-1}$ for both types of halo which places corotation for the bar at $r_L \simeq 1.23r_B$, in excellent agree-

ment with the value found by Lindblad, Lindblad & Athanassoula (1996) and consistent with most determinations of this ratio for other galaxies (*e.g.* Aguerri, Debattista & Corsini 2003).

Our estimated mass-to-light ratio values are $\Upsilon_I \simeq 2.50 \pm 1$ for the isothermal halo models and $\Upsilon_I = 1.75 \pm 1$ for the NFW halo. While the constraints are disappointingly loose, the preferred mass-to-light ratio in both our halo models, $\Upsilon_I \simeq 2.0 \pm 1$, is consistent with that obtained by Weiner *et al.* (2001) and Weiner (2004) in two other cases. For NGC 1365, however, this value implies a massive, but not fully maximal, disk, and we do not find support for the disk-only model with no halo that was suggested by JvM95. Although such a model can reproduce the declining rotation curve (see their Fig. 24), the simulated gas flow produced by such a model (which in the I band is $\Upsilon \sim 3.75$) is quite strongly excluded.

The preferred value of Υ_I is nicely consistent with those obtained in the two previous studies using this method (Weiner *et al.* 2001; Weiner 2004), but suggest somewhat more massive disks than predicted by population synthesis models (Bell & de Jong 2001; Bell *et al.* 2003) for galaxies of these colors.

The halos of our two models required to fit the declining rotation curve in the outer disk are distinctly non-standard, however. The circular speed in the pseudo-isothermal model declines steadily outside the large core, while the NFW halo has a very high concentration and small scale radius. Even allowing for compression of the halo as the massive disk forms within it, the original NFW halo has $c \simeq 22$, $V_{200} \simeq 123$ kms. The total dark matter mass out to r_{200} in this case is less than three times our estimated disk mass, and the halo is quite unlike those predicted by LCDM models for a galaxy of this mass.

The disturbed distribution and kinematics of the gas in this galaxy clearly complicates our attempt to identify a preferred mass model. Its projected position near the center of the Fornax cluster, together with its velocity within 200 km s^{-1} of the cluster mean, suggest it is a cluster member. The disturbed nature of the outer HI distribution should not therefore be regarded as surprising. But the high central density of this massive galaxy should ensure that tidal forces have little influence on the inner part, where we indeed see that the bar and inner spirals are very pleasingly bi-symmetric in the I-band light. The existence of such strong asymmetries in the inner parts of the gas and dust is rather surprising, therefore.

The asymmetry in the dust distribution and the kinematic map, combined with the existence of a number of patches of H α emission with anomalous velocities all suggest that the agent that caused the disturbance was an infalling gas cloud. We cannot say whether the gas was an isolated intergalactic cloud not associated with a galaxy, or whether it could be a stream of debris from a gas-rich dwarf galaxy that had been tidally disrupted. The

anomalous velocities clearly suggest that the infalling gas has yet to be assimilated in the disk of NGC 1365.

We are grateful to Scott Trager for obtaining photometric images at the Las Campanas Observatory. We received invaluable help and advice with the optical data reductions from Tad Pryor and with the radio data reductions from Gustaaf van Moorsel and the NRAO staff. This work was supported by NSF grants AST-0098282 and AST-0507323 awarded to JAS.

REFERENCES

- Aguerri, J. A. L., Debattista, V. P. & Corsini, E. M. 2003, MNRAS, **338**, 465
- Alloin, D., Edmunds, M. G., Lindblad, P. o. & Pagel, B. E. J. 1981, A&A, **101**, 377
- Athanassoula, E., Bosma, A. & Papaioannou, S. 1987, A&A, **179**, 23
- Barnes, E. I., Sellwood, J. A., 2003, AJ, **125**, 1164
- Barnes, E. I., Sellwood, J. A. & Kosowsky, A. 2004, AJ, **128**, 2724
- Beck, R., Fletcher, A., Shukurov, A., Snodin, A., Sokoloff, D. D., Ehle, M., Moss, D. & Shoutenkov, V. 2005, A&A, **444**, 739
- Bell, E. F. & de Jong, R. 2001, ApJ, **550**, 212
- Bell, E. F., McIntosh, D. H., Katz, N. & Weinberg, M. D. 2003, ApJS, **149**, 289
- Binney, J. & Merrifield, M. 1998, *Galactic Astronomy*, (Princeton: Princeton University Press)
- Binney, J. & Tremaine, S. 1987, *Galactic Dynamics* (Princeton: Princeton University Press)
- Bissantz, N., Englmaier, P. & Gerhard, O. 2003, MNRAS, **340**, 949
- Boomsma, R., van der Hulst, T., Osterloo, T., Fraternali, F. & Sancisi, R. 2004, in IAU Symposium **217**, eds. P.-A. Duc, J. Braine & E. Brinks (San Francisco: ASP), 142
- Bosma, A. 1998, in *Galactic Halos*, ed. D. Zaritsky (San Francisco: ASP) **136**, p. 193
- Bottema, R. 1993, A&A, **275**, 16

- Bottema, R. 1997, A&A, **328**, 517
- Bottema, R., van der Kruit, P. C. & Freeman, K. C. 1987, A&A, **178**, 77
- Briggs, D. S. 1995, Ph.D. thesis, New Mexico Institute of Mining and Technology
- Bullock, J. S., Kolatt, T. S., Sigad, Y., Somerville, R. S., Kravtsov, A. V., Klypin, A. A., Primack, J. R. & Dekel, A. 2001, MNRAS, **321**, 559
- Casertano, S. 1983, MNRAS, **203**, 735
- Casertano, S. & van Gorkom, J. H. 1991, AJ, **101**, 1231
- Ciardullo, R., Durrell, P. R., Laychak, M. B., Herrmann, K. A., Moody, K., Jacoby, G. H. & Feldmeier, J. J. 2004, ApJ, **614**, 167
- Debattista, V. P. & Sellwood, J. A. 2000, ApJ, **543**, 704
- Duval, M. F. & Athanassoula, E. 1983, A&A, **121**, 297
- de Grijs, R., van der Kruit, P. C. 1996, A&AS, **117**, 19
- de Jong, R. S. 1996, A&A, **313**, 377
- de Jong, R. S. & Bell, E. F. 2007, “Island Universes – Structure and Evolution of Disk Galaxies”, p107 (astro-ph/0604391)
- de Vaucouleurs, G., de Vaucouleurs, A., Corwin, H. G., Jr., Buta, R. J., Paturel, G. & Fouque, P. 1991, Volume 1-3, XII (Berlin Heidelberg New York: Springer-Verlag)
- Dutton, A. A., van den Bosch, F. C., Dekel, A., Courteau, S. 2007, ApJ, **654**, 27
- Edmunds, M. G., Taylor, K. & Turtle, A. J. 1988, MNRAS, **234**, 155
- Emsellem, E., Greusard, D., Combes, F., Friedli, D., Leon, S., Pécontal, E., & Wozniak, H. 2001, A&A, **368**, 52
- Englmaier, P. & Gerhard, O. 1997, MNRAS, **287**, 57
- Erwin, P. 2004, A&A, **415**, 941
- Erwin, P. 2005, MNRAS, **364**, 283
- Fuchs, B. 2003, Ap&SS, **284**, 719
- Galliano, E., Alloin, D., Pantin, E., Lagage, P. O. & Marco, O. 2005, A&A, **438**, 803

- Giovanelli, R., Haynes, M. P., Salzer, J. J., Wegner, G., da Costa, L. N. & Freudling, W. 1994, *AJ*, **107**, 2036
- Giovanelli, R., Haynes, M. P., Herter, T., Vogt, N. P., Wegner, G., Salzer, J. J., da Costa, L. N. & Freudling, W. 1997, *AJ*, **113**, 22
- Gunn, J. E., Knapp, G. R. & Tremaine, S. D. 1979, *AJ*, **84**, 1181
- Helfer, T. T., Thornley, M. D., Regan, M. W., Wong, T., Sheth, K., Vogel, S. N., Blitz, L. & Bock, D. C.-J. 2003, *ApJS*, **145**, 259
- Holwerda, B. W., Gonzalez, R. A., Allen, R. J. & van der Kruit, P. C. 2005, *AJ*, **129**, 1381
- Jörsäter, S., Peterson, C. J., Lindblad, P. O. & Bokkenberg, A. 1984, *A&AS*, **58**, 507
- Jörsäter, S., van Moorsel, G. A. 1995, *AJ*, **110**, 2037
- Jungwiert, B., Combes, F. & Axon, D. J. 1997, *A&A*, **125**, 479
- Kamphuis, J. 1993, PhD thesis, University of Groningen
- Kamphuis, J. & Sancisi, R. 1993, *A&A*, **273**, L31
- Kranz, T., Slyz, A. & Rix, H.-W. 2003, *ApJ*, **586**, 143
- Kregel, M., van der Kruit, P. C. & de Grijs, R. 2002, *MNRAS*, **334**, 646
- Laine, S., Shlosman, I., Knapen, J. H. & Peletier, R. F. 2002, *ApJ*, **567**, 97
- Lake, G. & Feinswog, L. 1989, *AJ*, **98**, 166
- Landolt, A. U. 1992, *AJ*, **104**, 340
- Lindblad, P. O. 1978,
- Lindblad, P. O. 1999, *A&A Rev.*, **9**, 221
- Lindblad, P. O., Hjelm, M., Hoegbom, J., Jörsäter, S., Lindblad, P. A. B. & Santos-Lleo, M. 1996, *A&AS*, **120**, 403
- Lindblad, P. A. B., Lindblad, P. O. & Athanassoula, E. 1996, *A&A*, **313**, 65
- McGaugh, S. S. 2005, *ApJ*, **632**, 859
- Madore, B. F., *et al.* 1999, *ApJ*, **515**, 29

- Mathewson, D. S. & Ford, V. L. 1996, *ApJS*, **107**, 97
- Navarro, J. F., Frenk, C. S. & White, S. D. M. 1997, *ApJ*, **490**, 493
- Noordermeer, E., van der Hulst, J. M., Sancisi, R., Swaters, R. S. & van Albada, T. S. 2007, *MNRAS*, to appear (arXiv:astro-ph/0701731)
- Osterbrock, D. E. & Martel, A. 1992, *PASP*, **104**, 76
- Palunas, P. & Williams, T. B. 2000, *AJ*, **120**, 2884
- Pérez, I. 2007, *A&A*, to appear (arXiv:0710.2855)
- Pérez, I., Fux, R. & Freeman, K. 2004, *A&A*, **424**, 799
- Phillips, M. M., Edmunds, M. G., Pagel, B. E. J. & Turtle, A. J. 1983, *MNRAS*, **203**, 759
- Pizagno, J., *et al.* 2005, *ApJ*, **633**, 844
- Portinari, L., Sommer-Larsen, J. & Tantalo, R. 2004, *MNRAS*, **347**, 691
- Press, W. H., Flannery, B. P., Teukolsky, S. A. & Vetterling, T. A. 1992, *Numerical Recipes* (Cambridge: Cambridge Univ. Press)
- Roberts, W. W., Huntley J. M. & van Albada G. D. 1979, *ApJ*, **233**, 67
- Sackett, P. D. 1997, *ApJ*, **483**, 103
- Sakai, S., *et al.* 2000, *ApJ*, **529**, 698
- Sakamoto, K., Ho, P. T. P., Mao, R.-Q., Matsushita, S. & Peck, A. B. 2007, *ApJ*, **654**, 782
- Sandqvist, A., Jörsäter, S. & Lindblad, P. O. 1995, *A&A*, **295**, 585
- Schlegel, D. J., Finkbeiner, D. P. & Davis, M. 1998, *ApJ*, **500**, 525
- Sellwood, J. A. 1999, in *Galaxy Dynamics – A Rutgers Symposium*, eds. D. Merritt, J. A. Sellwood & M. Valluri (San Francisco: ASP) **182**, p. 351
- Sellwood, J. A. & McGaugh, S. S. 2005, *ApJ*, **634**, 70
- Sellwood, J. A. & Sparke, L. S. 1988, *MNRAS*, **231**, 25P
- Sellwood, J. A. & Wilkinson, A. 1993, *Rep. Prog. Phys.*, **56**, 173
- Spergel, D. N., *et al.* 2007, *ApJS*, **170**, 377

- Stark, A. A. & Brand, J. 1989, ApJ, **339**, 763
- Strutskie *et al.* 1997, in The impact of Large Scale Near-IR Sky Surveys, ed. F. Garzon *et al.* (Dordrecht:Kluwer), 25
- Teuben, P. J., Sanders, R. H., Atherton, P. D. & van Albada, G. D. 1986, MNRAS, **221**, 1
- van Albada, G. D. 1985, A&A, **142**, 491
- van Albada, T. S., Bahcall, J. N., Begeman, K. & Sancisi, R. 1985, ApJ, **295**, 305
- van Moorsel, G. A., Wells, D. C. 1985, AJ, **90**, 1038
- Verheijen, M. A. W., Bershad, M. A., Andersen, D. R., Swaters, R. A., Westfall, K., Kelz, A. & Roth, M. M. 2004, Astronomische Nachrichten, **325**, 151
- Wakker, B. P. & van Woerden, H. 1997, ARA&A, **35**, 217
- Weiner, B. J. 2004, in IAU Symp. 220, Dark Matter in Galaxies, ed. S. Ryder, D. J. Pisano, M. Walker & K. Freeman (Dordrecht: Reidel), 35
- Weiner, B. J., Williams, T. B., van Gorkom, J. H. & Sellwood, J. A. 2001, ApJ, **546**, 916
- Weiner, B. J., Sellwood, J. A. & Williams, T. B. 2001, ApJ, **546**, 931
- Williams, T. B., Caldwell, N. & Schommer, R. A. 1984, ApJ, **281**, 579
- Wozniak, H., Friedli, D., Martinet, L., Martin, P. & Bratschi, P. 1995, A&AS, **111**, 115

Table 1. Halo Parameters

Disk Υ_I	ρ_0	r_c	k	χ^2/N
b1025				
1.00	1433.20	1.45	2.61	0.92
1.50	420.20	2.64	3.00	0.92
2.00	184.70	3.72	3.50	0.91
2.50	81.20	5.16	4.78	0.93
3.00	67.20	4.60	5.0	0.99
b1075				
0.50	1422.16	1.58	2.62	0.97
0.75	784.56	2.11	2.77	0.96
1.00	346.08	3.19	3.10	0.92
1.25	354.20	3.01	3.05	0.87
1.50	241.21	3.55	3.27	0.86
1.75	173.99	4.02	3.51	0.86
2.00	126.70	4.51	3.81	0.87
2.25	91.30	5.06	4.29	0.89
2.50	62.55	5.72	5.0	0.92
2.75	56.43	5.41	5.0	0.97
3.00	49.10	4.87	5.0	1.06
3.25	49.92	4.06	5.0	1.21
3.50	18.16	3.87	5.0	1.36
3.75	2.02	1.36	5.0	1.70
b2050				
1.00	691.78	2.13	2.76	0.92
1.50	212.37	3.75	3.31	0.89
2.00	109.76	4.75	3.86	0.89
2.50	53.03	5.97	5.0	0.95
3.00	36.85	5.18	5.0	1.08
b2075				
1.00	381.17	2.96	2.98	0.90
1.50	166.99	4.20	3.44	0.86
2.00	90.10	5.14	3.98	0.90
2.50	43.60	6.31	5.0	1.00
3.00	30.49	5.23	5.0	1.18
b3075				
1.00	305.24	3.29	3.05	0.92
1.50	134.05	4.59	3.52	0.88
2.00	82.60	5.06	3.76	0.92
2.50	32.46	6.63	5.0	1.05
3.00	14.77	5.85	5.0	1.26

Note. — Dark matter halo parameters for five different bulge models. For models with $\Upsilon_I = 2.75$ and 3.00, the k parameter was fixed to 5 to avoid a sharp edges on the halo profile

Table 2. NFW Halo Parameters

Disk Υ_I	ρ_s	r_s	c	V_{200}	χ^2/N
0.50	829.96	2.90	67	135	0.92
0.75	802.80	2.84	66	131	0.93
1.00	710.48	2.87	63	127	0.90
1.25	685.32	2.80	62	122	0.92
1.50	662.08	2.71	61	116	0.93
1.75	641.40	2.61	61	111	0.96
2.00	563.16	2.61	58	106	0.98
2.25	182.60	3.94	38	105	1.16
2.50	190.40	3.55	38	96	1.15
2.75	208.36	3.08	40	86	1.15
3.00	240.20	2.54	42	75	1.17
3.25	229.16	2.22	41	64	1.26
3.50	173.00	1.85	37	48	1.33
3.75	0.36	2.17	3	4	1.42

Note. — Dark matter halo parameters for NFW halo. The densities are in $10^{-3} M_{\odot} pc^{-3}$, the radii in kpc, and V_{200} is in $km\ s^{-1}$.

Table 3. Comparison with Population Synthesis

Galaxy	B	V	I	Pred 1 Υ_I	Pred 2 Υ_I	Dynamical Υ_I
NGC 4123	11.97	11.38	10.36	1.22	1.48	2.25 ± 0.25
NGC 3095	11.72	11.16	10.10	1.16	1.67	2.00 ± 0.25
NGC 1365		9.21	8.05		2.28	2.00 ± 1.00

Note. — Our galaxy isophotal magnitudes in 3 color bands corrected for internal and foreground extinction. Prediction 1 Υ_I is from B-V color using Bell *et al.* (2003) table 7. Prediction 2 Υ_I from V-I color using Bell & de Jong (2001) table 1. Our dynamical estimate of Υ_I .